

Numerical approximation of a 3D mechanochemical interface model for skin patterning[☆]

Luis Miguel De Oliveira Vilaca^{a,b}, Michel C. Milinkovitch^{a,b},
Ricardo Ruiz-Baier^{c,d,*}



^a Laboratory of Artificial & Natural Evolution (LANE), Department of Genetics and Evolution, University of Geneva, 4 Boulevard d'Yvoi, 1205 Geneva, Switzerland

^b SIB Swiss Institute of Bioinformatics, Geneva, Switzerland

^c Mathematical Institute, University of Oxford, Oxford OX2 6GG, United Kingdom

^d Laboratory of Mathematical Modelling, Institute of Personalised Medicine, Sechenov University, Russian Federation

ARTICLE INFO

Article history:

Received 3 May 2018

Received in revised form 10 January 2019

Accepted 16 January 2019

Available online 4 February 2019

Keywords:

Elasticity-diffusion problem

Interface coupling

Pattern formation

Skin appendage modelling

Finite element methods

Adaptive time stepping

ABSTRACT

We introduce a model for the mass transfer of molecular activators and inhibitors in two media separated by an interface, and study its interaction with the deformations exhibited by the two-layer skin tissue where they occur. The mathematical model results in a system of nonlinear advection-diffusion-reaction equations including cross-diffusion, and coupled with an interface elasticity problem. We propose a Galerkin method for the discretisation of the set of governing equations, involving also a suitable Newton linearisation, partitioned techniques, non-overlapping Schwarz alternating schemes, and high-order adaptive time stepping algorithms. The experimental accuracy and robustness of the proposed partitioned numerical methods is assessed, and some illustrating tests in 2D and 3D are provided to exemplify the coupling effects between the mechanical properties and the advection-diffusion-reaction interactions involving the two separate layers.

© 2019 The Authors. Published by Elsevier Inc. This is an open access article under the CC BY license (<http://creativecommons.org/licenses/by/4.0/>).

1. Introduction and modelling considerations

Reliable modelling of mechanochemical properties of composite materials is of key importance in a variety of engineering, material science and life science applications. These include tissue engineering, wound healing manipulation, bone fracture repair, design of photovoltaic devices, polymer adhesion, and many others. Of special interest to us are the two-way interactions between, on one hand, biological tissue deformation and, on the other hand, migration and proliferation of certain cell types during organismal development.

One application of such a general model is the study of the vertebrate skin appendages development and evolution, especially their diversity of forms (such as hairs, spines, feathers, and scales; [22,36,37]), and spatial organisations. Note that we have recently established that all skin appendages are homologous structures developing from an anatomical placode and associated signalling molecules [14].

[☆] This work was partially supported by grants from the Swiss National Science Foundation (FNSNF, grants 31003A_179431 and SINERGIA CRSI13_132430), by the SystemsX.ch initiative (project Epi-PhysX); and by the Engineering and Physical Sciences Research Council (EPSRC, research grant EP/R00207X/1).

* Corresponding author at: Mathematical Institute, University of Oxford, Oxford OX2 6GG, United Kingdom.

E-mail addresses: LuisMiguel.DeOliveiraVilaca@unige.ch (L.M. De Oliveira Vilaca), Michel.Milinkovitch@unige.ch (M.C. Milinkovitch), RuizBaier@maths.ox.ac.uk (R. Ruiz-Baier).

Turing proposed in his seminal work [56] that pattern formation in biological systems could be explained by a system of diffusion and interacting chemicals that he called ‘morphogens’. Many subsequent studies [33,51,49] investigated biological patterning in the framework of such purely chemical reaction-diffusion models. However, as already suggested by Turing [56], mechanical aspects might also be relevant to biological patterning processes. During the last decade, biological experiments have clearly indicated that not only chemical (pattern of morphogen concentrations), but also mechanical (stresses and strains), parameters are key to skin development [1,22,42,55] and are synchronised during embryonic development [40]. For example, it has been recently shown [52,26] that the patterning of avian feathers involves the integration of mechanical and reaction-diffusion-taxis elements. Indeed, the local production of FGF by the embryonic skin epithelium stimulates mesenchymal cell aggregation which, in turn, activates the expression of BMP4 (an inhibitor of FGF expression). However, cell aggregation also mechanically deforms the embryonic epidermis. The resulting local compression triggers re-localisation of β -catenin from the epidermal cell membrane to the nucleus, mimicking the effect of canonical WNT signalling, hence amplifying epithelial FGF20 production. In other words, the positive loop of activation of epidermal FGF expression requires transduction, by β -catenin, of the mechanical stimulus generated by local mesenchymal cell clustering.

Although the full detailed underlying mechanisms are still incompletely understood, authors have attempted to integrate both chemical and mechanical parameters in their mathematical models of skin patterning [41,43]. The various proposed mechanochemical models differ by the nature of the interactions between morphogen concentration and mechanics. For instance, while in [39,47] mechanical responses are directly triggered by chemical signalling, other models [38,39] propose that migration of cells directly generate local forces on the tissue. Such interactions between cells and morphogens can be complemented with chemical and mechanical exchanges between the two layers (dermis and epidermis) that constitutes the skin [12,50]. In one example [5], a three-chemical species model of limb bud development integrates growth velocity of the tissue normal to the limb surface and that directly depends on the local concentration of fibroblast growth factor. Other models consider the tissue growth as a liquid displacement, or aggregation of cells is the result of a chemical pre-pattern.

Here we focus on the computational modelling of mechanochemical interactions (inspired by [12] and [50]) based on simple reaction-diffusion systems governing the relations between, on one hand, the concentration of morphogenic proteins and cells densities and, on the other hand, mechanical stresses and strains. The mathematical description proposed in these two references is sufficiently general to be applied to multiple biological contexts (e.g., angiogenesis, fingerprint formation, cartilage condensation [41]), justifying the numerical algorithm presented here. Experimental evidence shows that the skin short-term and low-amplitude response to mechanical stimuli is that of an elastic solid [13]. We therefore assume that the two-layer domain of the skin (dermis and epidermis) can deform according to its inherent mechanical response, and that it is affected isotropically via an internal force that depends on the signalling factors. In addition, given the long spatio-temporal scale of the organismal developmental process, short-term fluctuations and inertial effects can probably be safely discarded to simplify the mathematical model [38]. We therefore adopt the two following fundamental assumptions: (i) the equilibrium of forces in the system is established by a quasi-static balance of linear momentum, and (ii) chemical species, governed by an advection-diffusion reaction (ADR) system, affect the medium deformation (through coupling functions). The chemical species’ dynamics represents the spatio-temporal evolution of two morphogenic proteins and/or of cells that trigger and control the internal forces affecting the momentum balance. In turn, cell motion induces local and global traction forces on the elastic body, leading to substrate deformations [42]. We point out that cell motility depends on different factors that include kineses (increase in motile activity without any directional component), taxes (directed motion up or down a gradient), and guidances (motion directed by substratum cues, also called contact guidance) [39] that can also act locally or globally. Although long-range effects can be implemented through high-order spatial derivatives (appearing in the ADR or force conservation equations), we will here incorporate only short-range effects because our focus is on the numerical and algorithmic aspects of interface problems (such as the dermis-epidermis interactions in the skin).

As suggested elsewhere [12], here we distinguish between the two very different cellular dynamics of the dermis and the epidermis. Whereas we adopted a general logistic growth mitotic rate and non-negligible short range cell diffusion [40] in the dermis, we account for a zero production rate of cells and very small diffusivities in the equations governing epidermal variables [1,50]. This difference of treatment in the two tissues is justified by their respective structures: cells in epidermal tissue form sheets of adjoined interacting cells, while mesenchymal cells in the dermis are more mobile and separated by substantial extracellular matrix. However, as epidermal cells are not completely attached to each other and can rearrange topologically [1], we assume in both dermis and epidermis that all diagonal terms in the diffusivity matrices are strictly positive.

Regarding the interface problem between dermis and epidermis, we considered multiple methods for numerical approximation of linear elasticity using mixed finite elements: parallel and sequential Schwarz iterations using various interface conditions based on boundary element-finite couplings [20], hp -mortar [8], Nitsche [7], multiscale settings [10], or matching interface algorithms [58]. We finally chose a Schwarz iteration method with domain decomposition where the coupled set of mechanochemical equations is solved separately on each side of the interface, imposing mixed-type (Robin) boundary conditions, i.e., both fluxes and density values are equal in both tissues at their interface. A rich body of literature deals with choosing the weighting coefficients on the Robin interface conditions in order to optimise the convergence of the alternating Schwarz algorithms under different scenarios (see e.g. [11,18,23,46] and references therein). As the optimal weighting scheme tends to be problem-dependent and might change substantially for diffusion, elasticity, or fluid-oriented problems, we will only describe general schemes and mention which specific weighting best suits the problems we investigate here.

Here, we define a family of finite element methods for the semi-discretisation of the problem, where the classical MINI-element [4] is used for the approximation of both displacement and pressure on each subdomain, whereas piecewise linear and continuous elements are used to discretise the vector of species concentration. Concerning the fully-discrete (spatial and time discretisation) scheme for the model problem, we apply an adaptive time-stepping strategy based on diagonally-implicit Runge–Kutta methods. This so-called TR-BDF2 method was introduced in the context of electronic circuit simulation [6] (see also [9,27,16] for further details) and has the advantage of using the same Newton iteration matrix to solve different temporal stages within a time step, a particularly interesting feature when addressing large systems of ODEs. The step size adaptivity exploits classical automatic control techniques used in the integration of so-called stiff systems [24,25], i.e., problems that tend to be numerically unstable.

This article is organised in the following manner. The remainder of this section contains preliminary notation and generalities to be used throughout the paper. Section 2 provides a detailed description of the differential equations constituting the model problem, with special emphasis on the coupling occurring at the interface. In Section 3, we introduce the Galerkin method, we present the adaptive time discretisation, and we specify algorithmic considerations. Section 4 contains a collection of computational tests focusing on the accuracy of the numerical schemes and on the suitability of the model equations to represent mechanochemical problems. We close with a summary and discuss potential extensions of the model in Section 5.

Throughout the paper, we let $\Omega \subset \mathbb{R}^d$, $d \in \{2, 3\}$ denote a deformable body with polyhedral boundary $\partial\Omega$, and denote by \mathbf{v} the outward unit normal vector on $\partial\Omega$. Moreover, given a generic domain $\mathcal{D} \in \mathbb{R}^d$, $d \in \{2, 3\}$, for two vectorial functions $\mathbf{u}, \mathbf{v} \in L^2(\mathcal{D})^d$ will denote their inner product as $(\mathbf{u}, \mathbf{v})_{\mathcal{D}} = \int_{\mathcal{D}} \mathbf{u} \cdot \mathbf{v} \, d\mathbf{x}$, whereas if \mathcal{S} is a $(d-1)$ -dimensional surface then their pairing will be written as $\langle \mathbf{u}, \mathbf{v} \rangle_{\mathcal{S}} = \int_{\mathcal{S}} \mathbf{u} \cdot \mathbf{v} \, ds$. In addition, by $\mathbb{P}_r(\mathcal{D})$ we will denote the space of polynomial functions of degree $s \leq r$ defined on the domain \mathcal{D} , and \mathbf{I} stands for the identity matrix in $\mathbb{R}^{d \times d}$. Finally, we will employ $\mathbf{0}$ to denote a generic null vector or the zero operator.

2. Set of governing equations

Linear elastic solids. We assume that the domain Ω is disjointly divided into two connected subdomains (with different material properties) denoted by Ω^D and Ω^E , respectively, whose intersection constitutes the interface between the regions and is denoted $\Sigma = \partial\Omega^D \cap \partial\Omega^E$. On $\partial\Omega^E$ we define a part of the boundary related to the exposed surface, denoted as Γ (see Fig. 2.1).

This heterogeneity of the skin (corresponding to the presence of an homogeneous *dermis* and an homogeneous *epidermis*, occupied by Ω^D and Ω^E , respectively) is accounted for by the spatially-dependent (but locally constant) Lamé coefficients

$$\lambda = \begin{cases} \lambda^D & \text{in } \Omega^D, \\ \lambda^E & \text{in } \Omega^E, \end{cases} \quad \mu = \begin{cases} \mu^D & \text{in } \Omega^D, \\ \mu^E & \text{in } \Omega^E. \end{cases}$$

We also suppose that the two-layered elastic medium is nearly incompressible, so, in view of avoiding the well-known phenomenon of volumetric locking (inability of some discrete spaces to approximate the true displacement while satisfying incompressibility, see e.g. [8]), a mixed formulation is adopted in terms of displacements \mathbf{u}^* and the pressure $p^* = -\lambda^* \operatorname{div} \mathbf{u}^*$, with $* \in \{D, E\}$ (although the interpretation of p as pressure holds exclusively in the incompressibility limit where λ^*/μ^* takes on quite large values). For all $0 < t < T$, and given a body force \mathbf{f} (whose specific form depends on the vector \mathbf{w} ; see equation (2.5) below) applied on each domain, we resolve the displacement / pressure pair $(\mathbf{u}^*(t), p^*(t)) : \Omega^* \rightarrow [\mathbb{R}^d \times \mathbb{R}]$ on each subdomain, satisfying spring conditions at the surface boundary (Robin conditions), having clamped boundaries elsewhere, and assuming an adhesion condition at the interface (matching displacements and preservation of traction forces imply continuity of the medium across Σ). Then the global linear Navier–Lamé problem adopts the form

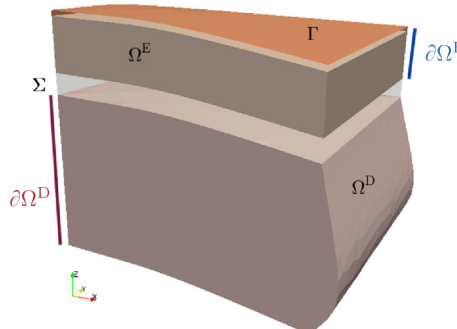


Fig. 2.1. Schematic representation of dermis and epidermis layers separated by the interface Σ and an exposed epidermic surface is denoted by Γ .

$$\begin{aligned}
-\operatorname{div}(2\mu^*\boldsymbol{\varepsilon}(\mathbf{u}^*) - p^*\mathbf{I}) &= \mathbf{f}(\mathbf{w}^*) && \text{in } \Omega^* \times (0, T), \\
p^* + \lambda^* \operatorname{div} \mathbf{u}^* &= 0 && \text{in } \Omega^* \times (0, T), \\
\boldsymbol{\sigma}^E \mathbf{v} + \alpha^E \mathbf{u}^E &= \mathbf{0} && \text{on } \Gamma \times (0, T), \\
\mathbf{u}^* &= \mathbf{0} && \text{on } \partial\Omega \setminus \Gamma \times (0, T), \\
\boldsymbol{\sigma}^D \mathbf{v} &= \boldsymbol{\sigma}^E \mathbf{v}, \quad \mathbf{u}^D = \mathbf{u}^E && \text{on } \Sigma \times (0, T),
\end{aligned} \tag{2.1}$$

where $\boldsymbol{\varepsilon}(\mathbf{u}^*) = \frac{1}{2}(\nabla \mathbf{u}^* + \nabla \mathbf{u}^{*T})$ is the tensor of infinitesimal strains (symmetric gradient of displacement), $\boldsymbol{\sigma}^* = 2\mu^*\boldsymbol{\varepsilon}(\mathbf{u}^*) - p^*\mathbf{I}$ is the Cauchy stress tensor, and $\alpha^* > 0$ is the Robin coefficient. The extension to non-homogeneous displacement conditions ($\mathbf{u}|_{\partial\Omega} \neq 0$) can be handled in a standard way by adding suitable liftings on the data. Below, we use the asterisk superscript $*$ $\in \{D, E\}$ to denote quantities related to each subdomain, and we adopt the convention that the unit normal vector \mathbf{v} on the interface is pointing from Ω^D to Ω^E .

We stress that modelling the development of soft tissue and cells, in terms of mechanical dynamic behaviour is still an active area of research [2,57]. Biological tissues, depending on the nature of the constituent cells, present a large variability in their elastic properties (including viscous, nonlinear, or nonlocal effects) which can change substantially through spatio-temporal scales [35,44,57]. Some recent analyses were based on nonlinear St. Venant–Kirchhoff descriptions [35], including viscoelastic terms [2,39,54,56], and even fluid dynamics, as mentioned in [57]. A general consensus on how to represent mechanical properties of the skin tissue under morphogenesis is not yet available. Hence, our description will be restricted to classical linear elastic materials because it accurately represents small tissue deformations manifested during the first stage of skin appendage formation.

Advection-diffusion-reaction equations on an underlying deforming medium. Let us focus on the spatio-temporal interaction of the densities of m species $\mathbf{w} = (w_1, \dots, w_m)$. We assume that all constituent species are equi-present at each spatial point (i.e., they are spatially continuous), so applying the Reynolds transport theorem to their mass conservation (assuming zero-flux boundary conditions at the surface Γ and continuity of fluxes and densities at the interface) leads to the system

$$\begin{aligned}
\partial_t \mathbf{w}^* + (\partial_t \mathbf{u}^* \cdot \nabla) \mathbf{w}^* - \operatorname{div}(\mathbf{M}^* \nabla \mathbf{w}^*) &= \mathbf{G}(\mathbf{w}^*) + \mathbf{g}(\mathbf{u}^*) && \text{in } \Omega^* \times (0, T), \\
\mathbf{M}^* \nabla \mathbf{w}^* \mathbf{v} &= \mathbf{0} && \text{on } \partial\Omega \times (0, T), \\
\mathbf{M}^D \nabla \mathbf{w}^D \mathbf{v} &= \mathbf{M}^E \nabla \mathbf{w}^E \mathbf{v}, \quad \mathbf{w}^D = \mathbf{w}^E && \text{on } \Sigma \times (0, T).
\end{aligned} \tag{2.2}$$

Here $\mathbf{M}^* \in \mathbb{R}^{m \times m}$ is a (not necessarily diagonal, but positive definite) tensor of self- and cross-diffusion rates, $\mathbf{G} : \Omega \rightarrow \mathbb{R}^m$ is a vectorial function containing the reaction kinetics of the system and representing the production and degradation of species concentration on each subdomain Ω^D, Ω^E ; and the term \mathbf{g} encodes an additional coupling contribution (detailed in equation (2.5) below). The system is endowed with adequate initial conditions for \mathbf{w}^* , and the general form (2.2) accommodates either dimensional or dimensionless descriptions.

We focus mainly on two levels of model complexity. Firstly, we define a simple two-variable activator-inhibitor model with quadratic reaction terms due to Gierer–Meinhardt (cf. [21]):

$$\mathbf{G}(\mathbf{w}^*) = \begin{pmatrix} \rho_2 \left(\rho_0 + \rho_1 \frac{(w_1^*)^2}{w_2^*} \right) - \rho_3 w_1^* \\ \rho_4 (w_1^*)^2 - \rho_5 w_2^* \end{pmatrix}, \tag{2.3}$$

where w_1^* is the short-range autocatalytic substance and w_2^* is the long-range antagonist; and the ρ_i 's are positive model parameters.

Second, we introduce a more general model of skin appendages development where w_1^* is the cell density, w_2^* is the density of the extracellular matrix, and w_3^*, w_4^* are the concentrations of two morphogens signalling chemical compounds. All quantities are assumed to diffuse, so none of the diagonal terms in \mathbf{M}^* is zero (nevertheless, self-diffusion for cell concentration in the epidermis and the matrix density in the two tissues, will be very small in comparison to the other values in the diagonal of \mathbf{M}^E); and, for sake of simplicity and the fact that the present study will concentrate on numerical aspects, we discard higher order terms (derivative with order higher than two) representing haptotaxis and non-local effects in the cell migration fluxes. The reactions consist in a logistic relation for the mitotic rate, a zero rate of matrix material secretion, and the production, as well as degradation, of morphogens:

$$\mathbf{G}(\mathbf{w}^D) = \begin{pmatrix} r_1 w_1^D (r_0 - w_1^D) \\ 0 \\ r_2 w_1^D - r_3 w_3^D \\ -r_4 w_1^D w_4^D \end{pmatrix}, \quad \mathbf{G}(\mathbf{w}^E) = \begin{pmatrix} 0 \\ 0 \\ -r_5 w_1^E w_3^E \\ r_6 w_1^E - r_7 w_4^E \end{pmatrix}, \tag{2.4}$$

where r_0 is the maximum cell density, and r_i 's are positive model constants. The specifications in (2.4) have been adapted from the skin pattern formation model proposed in [12]. Similar models can be found in the context of cell migration, angiogenesis, follicle differentiation, or mesenchymal morphogenesis (see e.g. [1,34,37,43]).

Coupling mechanisms. Extensive experimental evidence indicates that both biochemical and mechanical processes work in concert during pattern formation (see for instance [1,2,22,28,35,52]). In the specific context of skin appendages formation, signalling pathways control cell movements that eventually lead to mechanical tissue deformation due to cell aggregation [1,22,52]. These interactions can be represented by diverse local or non-local processes including advection, cytoskeleton regulation, chemical gradients, active stress, strain dependent diffusivity, and many others [40,38]. In the present model we opt for including only local variations of the ADR and mechanical variables. This simplification rules out some phenomena such as inter-cellular force transmission through cytoskeleton, nonlinear interactions (e.g., cells sensing, through filopodia, long-range variations), or anisotropy effects, which can be of special importance in some biological contexts [12,34]. Nonetheless, as suggested in [38], local models such as the one we use here, may suffice to reproduce accurately a variety of mechanical processes without the need for additional constitutive relations.

The PDE-based model (2.1)–(2.2) (written in Eulerian form and solving for displacements, solid pressure, and molecular variables) assumes that changes in the chemical concentrations do not affect the mechanical properties of the solid, nor the Lamé constants; the species only act as forcing terms on the momentum balance, i.e., the intensity of the deformation will depend locally on the gradient of the species concentrations. Conversely, we here suppose that the body deformation affects the species dynamics by means of advection and through the term $\mathbf{g}(\mathbf{u}^*)$ on the right-hand side in (2.2), carrying local information about the medium dilation. Therefore, we set

$$\mathbf{f}(\mathbf{w}^*) = c_f^* \sum_{i=1}^m \nabla w_i^*, \quad \mathbf{g}(\mathbf{u}^*) = c_g^* \operatorname{div} \mathbf{u}^* \begin{pmatrix} 1 \\ \vdots \\ 1 \end{pmatrix}, \quad (2.5)$$

where c_f^*, c_g^* are model parameters. Note that the form of \mathbf{f} is equivalent to considering a stress component depending on the concentrations of some w_i^* , that is $\boldsymbol{\sigma}^* = \boldsymbol{\sigma}_{\text{eff}}^* + w_i^* \mathbf{I}$, where $\boldsymbol{\sigma}_{\text{eff}}^*$ is an effective elastic stress. Similar coupling conditions can be found in [19,31,48].

2.1. Weak formulation for the multidomain problem

Multiplying (2.1)–(2.2) by suitable test functions, integrating by parts over each region Ω^* , and exploiting the boundary and interface conditions, we arrive at the following primal-mixed variational problem associated to the elasticity-ADR problem: For $t > 0$, find $(\mathbf{u}^*(t), p^*(t), \mathbf{w}^*(t)) \in \mathcal{V}^* \times \mathcal{Q}^* \times \mathcal{Z}^*$ such that

$$\begin{aligned} a(\mathbf{u}^*(t), \mathbf{v}) + b(p^*(t), \mathbf{v}) + \alpha^* \langle \mathbf{u}^*(t), \mathbf{v} \rangle_{\Gamma} &= F(\mathbf{w}^*; \mathbf{v}) \quad \forall \mathbf{v} \in \mathcal{V}^*, \\ b(q, \mathbf{u}^*(t)) - c(p^*(t), q) &= 0 \quad \forall q \in \mathcal{Q}^*, \\ (\partial_t \mathbf{w}^*(t), \mathbf{z})_{\Omega^*} + C(\mathbf{u}^*(t), \mathbf{w}^*(t); \mathbf{z}) + d(\mathbf{w}^*(t), \mathbf{z}) &= G(\mathbf{w}^*; \mathbf{z}) \quad \forall \mathbf{z} \in \mathcal{Z}^*, \end{aligned} \quad (2.6)$$

where α^E is the coefficient associated to the Robin boundary condition at the surface, and the specific boundary treatment implies that adequate functional spaces are

$$\mathcal{V}^* := H_0^1(\Omega^*)^d = \{\mathbf{v} \in H^1(\Omega^*)^d : \mathbf{v}|_{\partial\Omega \setminus \Gamma} = \mathbf{0}\}, \quad \mathcal{Q}^* = L^2(\Omega^*), \quad \mathcal{Z}^* = H^1(\Omega^*)^m.$$

Linear and nonlinear forms (lowercase and uppercase, respectively) involved in (2.6) are defined as

$$\begin{aligned} a(\mathbf{u}, \mathbf{v}) &:= 2\mu^*(\boldsymbol{\epsilon}(\mathbf{u}), \boldsymbol{\epsilon}(\mathbf{v}))_{\Omega^*}, \quad b(q, \mathbf{v}) := -(q, \operatorname{div} \mathbf{v})_{\Omega^*}, \quad c(p, q) := \frac{1}{\lambda^*}(p, q)_{\Omega^*}, \\ C(\mathbf{u}(t), \mathbf{w}; \mathbf{z}) &:= ([\partial_t \mathbf{u} \cdot \nabla] \mathbf{w}, \mathbf{z})_{\Omega^*}, \quad d(\mathbf{w}, \mathbf{z}) := (\mathbf{M}^* \nabla \mathbf{w}, \nabla \mathbf{z})_{\Omega^*}, \\ F(\mathbf{w}; \mathbf{v}) &:= (\mathbf{f}(\mathbf{w}), \mathbf{v})_{\Omega^*}, \quad G(\mathbf{u}, \mathbf{w}; \mathbf{z}) := (\mathbf{G}(\mathbf{w}) + \mathbf{g}(\mathbf{u}), \mathbf{z})_{\Omega^*}. \end{aligned}$$

The unique solvability of (2.6) has not yet been addressed in the literature, however related results concerning the coupling of linearised mechanics and reaction-diffusion systems have been addressed in the context of cardiac and plant cell biomechanics [3,45].

Treating the interface: a non-overlapping continuous Schwarz method. As mentioned previously, the treatment of the interface (here, between the epidermis and dermis) is an important issue for interacting media problems and this paragraph will focus on its realisation. Regarding the geometric separation between the problems defined on each side of the interface, we remark that (2.6) is valid in particular if we consider a solution globally defined in Ω . Nevertheless, in the discrete case we aim at solving two separate problems on each subdomain and therefore we require to impose jump conditions in an

adequate manner. We adopt a non-overlapping Schwarz iteration based on Robin–Robin type interface conditions for the ADR system

$$\mathcal{R}(\mathbf{w}^D) := \mathbf{M}^D \nabla \mathbf{w}^D + K^D \mathbf{w}^D = \mathbf{M}^E \nabla \mathbf{w}^E + K^E \mathbf{w}^E =: \mathcal{R}(\mathbf{w}^E) \quad \text{on } \Sigma \times (0, T), \quad (2.7)$$

where $\mathcal{R}(\cdot)$ denotes the Robin transmission operator, and K^D, K^E are nonnegative acceleration constants satisfying $K^D + K^E > 0$ (see, for instance [32] and [15]). On the other hand, the adhesion interface condition featured by the elasticity problem is incorporated through the following relation

$$\mathcal{S}(\mathbf{u}^D, p^D) := \boldsymbol{\sigma}^D \mathbf{v} + J^D \mathbf{u}^D = \boldsymbol{\sigma}^E \mathbf{v} + J^E \mathbf{u}^E =: \mathcal{S}(\mathbf{u}^E, p^E) \quad \text{on } \Sigma \times (0, T), \quad (2.8)$$

where $\mathcal{S}(\cdot, \cdot)$ is a transmission operator associated to the elasticity problem, and $J^* > 0$ is another acceleration constant. The classical iterative Schwarz algorithm (still continuous and still nonlinear) then reads: For $t > 0$ and for $\ell = 0, \dots$, find $(\mathbf{u}^{*,\ell+1}, p^{*,\ell+1}, \mathbf{w}^{*,\ell+1}) \in \mathcal{V}^* \times \mathcal{Q}^* \times \mathcal{Z}^*$ such that

$$\begin{aligned} a(\mathbf{u}^{*,\ell+1}, \mathbf{v}) + b(p^{*,\ell+1}, \mathbf{v}) + L^* \langle \mathbf{u}^{*,\ell+1}, \mathbf{v} \rangle_{\Sigma \cup \Gamma} &= F(\mathbf{w}^{*,\ell+1}; \mathbf{v}) + \langle \mathcal{S}^{\dagger,\ell}, \mathbf{v} \rangle_{\Sigma} \quad \forall \mathbf{v} \in \mathcal{V}^*, \\ b(q, \mathbf{u}^{*,\ell+1}) - c(p^{*,\ell+1}, q) &= 0 \quad \forall q \in \mathcal{Q}^*, \\ (\partial_t \mathbf{w}^{*,\ell+1}, \mathbf{z})_{\Omega^*} + C(\mathbf{u}^{*,\ell+1}, \mathbf{w}^{*,\ell+1}; \mathbf{z}) \\ + d(\mathbf{w}^{*,\ell+1}, \mathbf{z}) + K^* \langle \mathbf{w}^{*,\ell+1}, \mathbf{z} \rangle_{\Sigma} &= G(\mathbf{w}^{*,\ell+1}; \mathbf{z}) + \langle \mathcal{R}(\mathbf{w}^{\dagger,\ell}), \mathbf{z} \rangle_{\Sigma} \quad \forall \mathbf{z} \in \mathcal{Z}^*, \end{aligned} \quad (2.9)$$

where

$$L^* = \begin{cases} \alpha^E & \text{if } * = E \text{ and on } \Gamma, \\ J^* & \text{on } \Sigma, \\ 0 & \text{otherwise,} \end{cases}$$

and the superscript $\dagger \in \{D, E\}$ denotes quantities in the subdomain opposite to $*$. Here we have dropped the explicit time-dependence whenever clear from the context.

3. A finite element method and its splitting scheme

In this section we detail a Rothe-type strategy employed to numerically solve the set of governing equations (2.1)–(2.2). We first apply a discretisation in space written as a primal-mixed Galerkin formulation, which we later combine with fixed-point schemes and a Schwarz iterative algorithm decoupling the problem into four main blocks corresponding to each side of the interface, and to the elasticity and ADR equations. Then we discuss the time discretisation based on an adaptive scheme and operator splitting.

3.1. Nonlinear, partitioned Galerkin formulation

Let us denote by \mathcal{T}_h^* a shape-regular simplicial partition of Ω^* by triangles (for $d = 2$, or tetrahedra for $d = 3$) K of diameter h_K and define the global meshsize as $h := \max\{h_K : K \in \mathcal{T}_h^*\}$. For clarity of the presentation, we assume that the two meshes (associated with each subdomain) match at the interface. We will seek the approximation $(\mathbf{u}_h^*, p_h^*, \mathbf{w}_h^*)$ of $(\mathbf{u}^*, p^*, \mathbf{w}^*)$, in the finite dimensional product space

$$[\mathcal{V}_h^* \times \mathcal{Q}_h^* \times \mathcal{Z}_h^*] \subset [\mathcal{V}^* \times \mathcal{Q}^* \times \mathcal{Z}^*], \quad (3.1)$$

to be made precise below. Then, the semidiscrete Galerkin scheme associated to the Schwarz alternating algorithm (2.9) and a fixed-point decoupling of elasticity and ADR subproblems can be recast in the following partitioned form, iterated until convergence: For a given $t > 0$, and given $(\mathbf{u}_h^{*,\ell}, p_h^{*,\ell}, \mathbf{w}_h^{*,\ell}) \in \mathcal{V}_h^* \times \mathcal{Q}_h^* \times \mathcal{Z}_h^*$, find the next iteration $(\mathbf{u}_h^{*,\ell+1}, p_h^{*,\ell+1}, \mathbf{w}_h^{*,\ell+1})$ from the sequential system

$$\left\{ \begin{array}{l} (\partial_t \mathbf{w}_h^{D,\ell+1}, \mathbf{z}_h^D)_{\Omega^D} + C(\mathbf{u}_h^{D,\ell}, \mathbf{w}_h^{D,\ell+1}; \mathbf{z}_h^D) + d(\mathbf{w}_h^{D,\ell+1}, \mathbf{z}_h^D) \\ + K^D \langle \mathbf{w}_h^{D,\ell+1}, \mathbf{z}_h^D \rangle_{\Sigma} - G(\mathbf{w}_h^{D,\ell+1}; \mathbf{z}_h^D) = \langle \mathcal{R}_h^{E,\ell}, \mathbf{z}_h^D \rangle_{\Sigma} \quad \forall \mathbf{z}_h^D \in \mathcal{Z}_h^D, \end{array} \right. \quad (3.2)$$

$$\left\{ \begin{array}{l} a(\mathbf{u}_h^{D,\ell+1}, \mathbf{v}_h^D) + b(p_h^{D,\ell+1}, \mathbf{v}_h^D) + L^D \langle \mathbf{u}_h^{D,\ell+1}, \mathbf{v}_h^D \rangle_{\Sigma \cup \Gamma} = F(\mathbf{w}_h^{D,\ell}; \mathbf{v}_h^D) + \langle \mathcal{S}_h^{E,\ell}, \mathbf{v}_h^D \rangle_{\Sigma} \quad \forall \mathbf{v}_h^D \in \mathcal{V}_h^D, \\ b(q_h^D, \mathbf{u}_h^{D,\ell+1}) - c(p_h^{D,\ell+1}, q_h^D) = 0 \quad \forall q_h^D \in \mathcal{Q}_h^D, \end{array} \right. \quad (3.3)$$

$$\left\{ \begin{array}{l} (\partial_t \mathbf{w}_h^{E,\ell+1}, \mathbf{z}_h^E)_{\Omega^E} + C(\mathbf{u}_h^{E,\ell}, \mathbf{w}_h^{E,\ell+1}; \mathbf{z}_h^E) + d(\mathbf{w}_h^{E,\ell+1}, \mathbf{z}_h^E) \\ + K^E \langle \mathbf{w}_h^{E,\ell+1}, \mathbf{z}_h^E \rangle_{\Sigma} - G(\mathbf{w}_h^{E,\ell+1}; \mathbf{z}_h^E) = \langle \mathcal{R}_h^{D,\ell+1}, \mathbf{z}_h^E \rangle_{\Sigma} \quad \forall \mathbf{z}_h^E \in \mathcal{Z}_h^E, \end{array} \right. \quad (3.4)$$

Table 3.1
Butcher's tableau for the TR-BDF2 method.

| | | | |
|-----------|-----------------------------|-------------|-------------|
| 0 | 0 | 0 | 0 |
| 2γ | γ | γ | 0 |
| 1 | $1 - b_2 - \gamma$ | b_2 | γ |
| | $1 - b_2 - \gamma$ | b_2 | γ |
| | $1 - \hat{b}_2 - \hat{b}_3$ | \hat{b}_2 | \hat{b}_3 |

$$\begin{cases} a(\mathbf{u}_h^{E,\ell+1}, \mathbf{v}_h^E) + b(p_h^{E,\ell+1}, \mathbf{v}_h^E) + L^E \langle \mathbf{u}_h^{E,\ell+1}, \mathbf{v}_h^E \rangle_{\Sigma \cup \Gamma} = F(\mathbf{w}_h^{E,\ell+1}; \mathbf{v}_h^E) + \langle S_h^{D,\ell+1}, \mathbf{v}_h^E \rangle_{\Sigma} \quad \forall \mathbf{v}_h^E \in \mathcal{V}_h^E, \\ b(q_h^E, \mathbf{u}_h^{E,\ell+1}) - c(p_h^{E,\ell+1}, q_h^E) = 0 \quad \forall q_h^E \in \mathcal{Q}_h^E. \end{cases} \quad (3.5)$$

Note that the order in which these blocks are solved is arbitrary. We also note that the blocks (3.2), (3.5) still constitute nonlinear problems, that we solve through inner Newton iterations. Alternatively, one can commute the domain decomposition method and the nonlinear solvers, in such a way that the nonlinearly coupled set of equations can be solved monolithically on each subdomain. Further details on the choice we adopt here, are provided in Algorithm 1, below. Finally we remark that the sequential steps (3.2)–(3.5) can be regarded as a block Gauss–Seidel iteration applied to the fully monolithic differential-algebraic system.

For the discretisation of the elasticity equations in mixed form, we require the discrete spaces in (3.1) to be inf-sup stable. In our implementation we choose the so-called MINI elements [4], characterised by

$$\mathcal{V}_h^* := \{\mathbf{v} \in \mathbf{C}^0(\overline{\Omega^*}) : \mathbf{v}|_K \in [\mathbb{P}_1(K) + \mathbb{B}(K)]^d, K \in \mathcal{T}_h^*, \mathbf{v}|_{\partial\Omega \setminus \Gamma} = \mathbf{0}\}, \quad \mathcal{Q}_h^* := \{q \in C^0(\overline{\Omega^*}) : q|_K \in \mathbb{P}_1(K), K \in \mathcal{T}_h^*\},$$

where $\mathbb{B}(K)$ is the space of cubic bubble functions defined locally on an element K ; and we employ the space of conforming Lagrangian finite elements for the approximation of the species concentrations

$$\mathcal{Z}_h^* := \{\mathbf{z} \in \mathbf{C}^0(\overline{\Omega^*})^m : \mathbf{z}|_K \in \mathbb{P}_1(K)^m, K \in \mathcal{T}_h^*\}.$$

The discretisation (3.2)–(3.5) leads to the following system of equations

$$\mathbf{M}^* \dot{\mathbf{w}}^{*,l+1} + \mathbf{C}_u^* \mathbf{w}^{*,l+1} + \mathbf{D} \mathbf{w}^{*,l+1} - \mathbf{G}^*(\mathbf{w}^{*,l+1}) = \mathbf{0}, \quad (3.6)$$

$$\begin{cases} \mathbf{A}^* \mathbf{u}^{*,l+1} + (\mathbf{B}^*)^T \mathbf{p}^{*,l+1} - \mathbf{F}^*(\mathbf{w}^{*,\ddagger}) = \mathbf{0}, \\ \mathbf{B}^* \mathbf{u}^{*,l+1} - \mathbf{C} \mathbf{p}^{*,l+1} = \mathbf{0}, \end{cases} \quad (3.7)$$

where the superscript \ddagger may be replaced by the appropriate index associated to the Schwarz algorithm. We readily observe that only (3.6) is a nonlinear ODE system, whereas the matrix form of the elasticity sub-problem consists of a linear system. The subscript u in \mathbf{C}_u^* emphasises that the matrix is directly dependent on displacements.

3.2. Adaptive timestep scheme

The family of fully-discrete methods that we use here is based on adaptive, embedded Runge–Kutta schemes of order 2 and 3 (RK23). For a generic ODE system $\frac{d}{dt} v_h = L_h(v_h, \varphi_h(t))$, we recall that the main step in the classical RK23 scheme reads

$$\begin{aligned} v_h^{(i)} &= v_h^n + \sum_{j=1}^s a_{ij} \Delta t^n L_h(v_h^{(j)}, \varphi_h(t^n + c_j \Delta t^n)) \quad i = 1, 2, 3, \\ v_h^{n+1} &= v_h^n + \sum_{j=1}^s b_j \Delta t^n L_h(v_h^{(j)}, \varphi_h(t^n + c_j \Delta t^n)), \\ \hat{v}_h^{n+1} &= \hat{v}_h^n + \sum_{j=1}^s \hat{b}_j \Delta t^n L_h(v_h^{(j)}, \varphi_h(t^n + c_j \Delta t^n)), \end{aligned}$$

with $s = 3$ stages, and where the two approximations v_h, \hat{v}_h are of order $\mathcal{O}(p)$ and $\mathcal{O}(\hat{p})$, respectively. As in classical embedded RK methods, here the coefficients $\{a_{ij}, c_j\}$ coincide in both approximations; however the coefficients b_j differ in order to attain the expected convergence orders (in general one chooses $\hat{p} = p \pm 1$, cf. [24]). Even when the stability properties of the two schemes do not match, embedded RK methods provide a rather non-expensive estimator for the local error (of the less accurate solution) which is then directly used in the control of the timestep [24,25]. The specific description of the controller used here is presented in Algorithm 2, below.

The RK23 scheme is used together with the TR-BDF2 method (see [6]), which is a particular class of Diagonally Implicit Runge–Kutta (DIRK) methods (that is, $a_{ij} = 0$ for $i < j$, and at least one $a_{ii} \neq 0$) [24]. The scheme is characterised by the following Butcher's tableau reported in Table 3.1, where $b_2 = \frac{1-2\gamma}{4\gamma}$, $\hat{b}_2 = \frac{1}{12\gamma(1-2\gamma)}$, $\hat{b}_3 = \frac{2-6\gamma}{6(1-2\gamma)}$ and $\gamma = \frac{2-\sqrt{2}}{2}$.

As established in [27], the A-stability, the stiffly accuracy ($a_{sj} = b_j$, for $j = 1, \dots, s$), as well as the strong S-stability of the method are guaranteed by the coefficients used in Table 3.1. An appealing advantage of this scheme is that, for each step, only two implicit stages are required (where one can reuse the same Newton iteration matrix) while one stage is explicit. In this regard, the method is closely related to singly DIRK (SDIRK) methods (where all diagonal a_{ii} coefficients are equal and the first stage is explicit) [27]. In addition, TR-BDF2 falls in the class of First-Same-As-Last (FSAL) RK schemes, i.e. methods where the current explicit stage coincides with the last stage of the previous step, therefore decreasing the overall computational cost.

Based on Table 3.1, and considering $L_h = \mathbf{C}_u^* \mathbf{w}^* + \mathbf{D}\mathbf{w}^* - \mathbf{G}^*(\mathbf{w}^*)$ (where we have removed the Schwarz index whenever clear from the context), we can recast the intermediate stages as

$$\begin{aligned} \mathbf{w}^{*,(1)} &= \mathbf{w}^{*,n}, \\ \mathbf{M}^* \mathbf{w}^{*,(2)} &= \Delta t^n \gamma [-\mathbf{C}_u^* \mathbf{w}^{*,(2)} - \mathbf{D}\mathbf{w}^{*,(2)} + \mathbf{G}^*(\mathbf{w}^{*,(2)})] \\ &\quad + \Delta t^n \gamma [-\mathbf{C}_u^* \mathbf{w}^{*,(1)} - \mathbf{D}\mathbf{w}^{*,(1)} + \mathbf{G}^*(\mathbf{w}^{*,(1)})] + \mathbf{M}^* \mathbf{w}^{*,n}, \\ \mathbf{M}^* \mathbf{w}^{*,(3)} &= \Delta t^n \gamma [-\mathbf{C}_u^* \mathbf{w}^{*,(3)} - \mathbf{D}\mathbf{w}^{*,(3)} + \mathbf{G}^*(\mathbf{w}^{*,(3)})] \\ &\quad + \Delta t^n b_2 [-\mathbf{C}_u^* \mathbf{w}^{*,(2)} - \mathbf{D}\mathbf{w}^{*,(2)} + \mathbf{G}^*(\mathbf{w}^{*,(2)})] \\ &\quad + \Delta t^n (1 - b_2 - \gamma) [-\mathbf{C}_u^* \mathbf{w}^{*,(1)} - \mathbf{D}\mathbf{w}^{*,(1)} + \mathbf{G}^*(\mathbf{w}^{*,(1)})] + \mathbf{M}^* \mathbf{w}^{*,n}. \end{aligned}$$

These problems should be solved through Newton iterations before moving to the next timestep. Alternatively, and as suggested in [25], one can apply the change of variables $v_{z,h}^{(i)} := v_h^{(i)} - v_h^n$ and rewrite the problem accordingly. Doing so results in decreasing round-off errors and serves in reducing the cost to compute \hat{v}_h^{n+1} . We follow this approach and modify the superscripts $(1) \rightarrow n$, $(2) \rightarrow n + \gamma$ and $(3) \rightarrow new$, to obtain the following full discretisation of the ODE system:

$$\begin{aligned} \mathbf{w}^{*,n+\gamma} &= \gamma \mathbf{w}_z^{*,n+\gamma} + \gamma \mathbf{w}_z^{*,n} + \mathbf{w}^{*,n}, \\ \mathbf{w}^{*,new} &= \gamma \mathbf{w}_z^{*,new} + b_2 \mathbf{w}_z^{*,n+\gamma} + (1 - b_2 - \gamma) \mathbf{w}_z^{*,n} + \mathbf{w}^{*,n}, \end{aligned}$$

with

$$\begin{aligned} \mathbf{w}_z^{*,n+\gamma} &= (\mathbf{M}^*)^{-1} \Delta t^n [-\mathbf{C}_u^* \mathbf{w}^{*,n+\gamma} - \mathbf{D}\mathbf{w}^{*,n+\gamma} + \mathbf{G}^*(\mathbf{w}^{*,n+\gamma})], \\ \mathbf{w}_z^{*,new} &= (\mathbf{M}^*)^{-1} \Delta t^n [-\mathbf{C}_u^* \mathbf{w}^{*,new} - \mathbf{D}\mathbf{w}^{*,new} + \mathbf{G}^*(\mathbf{w}^{*,new})]. \end{aligned}$$

This nonlinear system is solved by means of Newton steps as follows

$$\begin{aligned} \mathbf{w}_{z,k+1}^* &= \mathbf{w}_{z,k}^* + \delta_{k+1} \mathbf{w}_z^*, \\ \left(\frac{1}{\Delta t^n} \mathbf{M}^* - \gamma \mathbf{J}^* \right)^{-1} \delta_{k+1} \mathbf{w}_z^* &= [-\mathbf{C}_u^* \mathbf{w}_k^* - \mathbf{D}\mathbf{w}_k^* + \mathbf{G}^*(\mathbf{w}_k^*)] - \frac{1}{\Delta t^n} \mathbf{M} \mathbf{w}_{z,k}^*, \end{aligned}$$

where

$$\mathbf{J}^* = -\mathbf{D}^* + \frac{\partial \mathbf{G}^*(\mathbf{w}_k^*)}{\partial \mathbf{w}^*} - \mathbf{C}_u^* = -\mathbf{D}^* + \mathbf{J}_{\mathbf{G}^*} - \mathbf{C}_u^*.$$

We finally point out that an additional reduction of computational cost occurs due to the fact that the local error $\text{err} = \hat{v}_h^{n+1} - v_h^{n+1}$ can be accessed by the simple relation

$$\text{err} = (\hat{b}_1 - b_1) \mathbf{w}_z^n + (\hat{b}_2 - b_2) \mathbf{w}_z^{n+\gamma} + (\hat{b}_3 - b_3) \mathbf{w}_z^{new},$$

avoiding the explicit storage and computation of \hat{v}_h^{n+1} .

3.3. Algorithmic details

Overall solution algorithm. The global numerical scheme to solve the mechanochemical model is summarised in Algorithm 1. After assigning suitable initial conditions $\mathbf{u}^{*,0} = \mathbf{0}$, $p^{*,0} = 0$, $\mathbf{w}^{*,0} = \mathbf{w}_0^*$, projected to the corresponding finite element spaces, we use the non-overlapping Schwarz method (3.2)–(3.5) to produce a solution until time T_f . Two important points stand out from this master algorithm. First, only the ADR equations are solved through the embedded RK method within the TR-BDF2 method (see Algorithm 1, Line 8, detailed in Algorithm 2), whereas the elasticity subproblem is

Algorithm 1 Overall solution algorithm for the mechanochemical problem.

```

1: Initialise the solution vectors  $\mathbf{u}^{*,0}$ ,  $\mathbf{p}^{*,0}$ ,  $\mathbf{w}^{*,0}$  and define  $\mathbf{w} \triangleq [\mathbf{w}^D, \mathbf{w}^E]^T$ ,  $\mathbf{w}_z \triangleq [\mathbf{w}_z^D, \mathbf{w}_z^E]^T$ 
2: while  $t \leq T_f$  do
3:    $\Delta t^{\min} = \epsilon |t|$ ,  $\Delta t^{\text{old}} = \Delta t$ ,  $\Delta t = \min(\Delta t^{\max}, \max(\Delta t^{\min}, \Delta t^{\text{old}}))$ 
4:   if  $\Delta t \neq \Delta t^{\text{old}}$  then
5:      $\mathbf{w}_z^n = \frac{\Delta t}{\Delta t^{\text{old}}} \mathbf{w}_z^{\text{old}}$ 
6:     needNewMJ  $\leftarrow$  true
7:   end if
8:   Compute  $t_{\text{new}}, \mathbf{w}^{\text{new}}, \mathbf{w}_z^{\text{new}}$  using TR-BDF2( $\mathbf{w}^n, \mathbf{w}_z^n, \Delta t, \beta_{\Delta t}$ ) ▷ See Algorithm 2
9:   for  $* \in \{D, E\}$  do procedure ELASTICITYsolver associated to (3.3) and (3.5)
10:     $\mathbf{F}^{*,n+1} = \mathbf{F}(\mathbf{w}^{*,n}, \mathbf{v}^{*,n+1} = -\frac{\mathbf{u}^{*,n}}{\Delta t})$ 
11:     $\begin{bmatrix} \mathbf{u}^{*,n+1} \\ \mathbf{p}^{*,n+1} \end{bmatrix} = \begin{bmatrix} \mathbf{A}^* & (\mathbf{B}^*)^T \\ \mathbf{B}^* & -\mathbf{C}^* \end{bmatrix}^{-1} \begin{bmatrix} \mathbf{F}^{*,n+1} \\ \mathbf{0} \end{bmatrix}$ 
12:     $\mathbf{v}^{*,n+1} = \mathbf{v}^{*,n+1} + \frac{\mathbf{u}^{*,n+1}}{\Delta t}$ 
13:    update Robin transmission conditions  $\mathcal{S}_h^*$  from (2.8)
14:  end for
15:  set  $n = n + 1$ ,  $t_{n+1} = t_{\text{new}}$ ,  $\mathbf{w}^{n+1} = \mathbf{w}^{\text{new}}$ ,  $\mathbf{w}_z^{n+1} = \mathbf{w}_z^{\text{new}}$ , and  $|\mathbf{w}^{n+1}|_2 = |\mathbf{w}^{\text{new}}|_2$ 
16:  Compute  $q = \left( \frac{\text{err}}{\text{RTOL}} \right)^{k_f}$ , ratio =  $\frac{\Delta t^{\max}}{\Delta t^{\text{old}}}$ , ratio =  $\min(\text{ratio}_{\max}, \max(\text{ratio}_{\min}, \text{ratio}))$ 
17:  if  $|\text{ratio} - 1| > \text{ratio}_{\min}$  then
18:     $\Delta t = \text{ratio} \cdot \Delta t$ ,  $\mathbf{w}_z^{n+1} = \text{ratio} \cdot \mathbf{w}_z^{n+1}$ 
19:    needNewMJ  $\leftarrow$  true
20:  end if
21: end while

```

solved by an implicit method (cf. Line 11 in Algorithm 1). Furthermore, the velocity in the advection term is approximated from the solid displacement using a backward Euler scheme (cf. Algorithm 1, Line 10 and 12). Second, the computation performed in Algorithm 1, Line 5 and 18, represents an alternative way of performing the explicit first stage of the RK scheme [27]. Such a rescaling must be executed at each modification of the timestep, so that one starts with an adequate value for \mathbf{w}_z when entering Line 8 of Algorithm 1. An additional benefit of the rescaling is that it improves the stability of the overall stiff problem, and at the same time avoids unnecessary function evaluations.

Adaptive Runge–Kutta method. The RK procedure is detailed in Algorithm 2 and it features a similar structure as the ODE solver ode23tb in MATLAB. Again, we highlight two major components: the one-step RK resolution and the adaptive setting of the timesteps. Line 2 in Algorithm 2 represents stage 2 of the RK method, i.e., the first implicit stage (S1). As the scheme is implicit, we initialise the tangent system associated with the Newton iteration. These matrices will actually be assembled only if the Boolean `mjcontrol` is true, and this switch is described in Algorithm 4, below. Should `mjcontrol` be false, the mass-Jacobian blocks are evaluated at each Newton step (see Algorithm 2, specifically Line 8). We also stress that the initial guess for the rescaled derivative $\mathbf{w}_z^{n+\gamma}$ can be simply taken as \mathbf{w}_z^n , since extrapolating the derivative of the interpolant from the previous step does not improve accuracy nor efficiency. Next, when updating the solutions we also change the Robin transmission conditions so that the Schwarz algorithm is performed at the same time (see Line 14 in Algorithm 2). In order to retrieve $\mathbf{w}_{z,k+1}^{\text{new}}$ and $\mathbf{w}_{k+1}^{\text{new}}$, a second Newton step is necessary within the implicit stage (S2), the particularity of which is the evaluation of the initial guess $\mathbf{w}_{z,0}^{\text{new}}$, by extrapolation of the derivatives of the cubic Hermite interpolant from t^n to $t^{n+\gamma}$ [27].

The algorithm also focuses on the automatic determination of each timestep, in view of the stability of the time integration of stiff problems. The process is designed to reject the overall step if one of the two implicit stages fails or if the local error is too large. The potential rejection at an implicit stage is monitored by the Boolean variables `rejectS1` and `rejectS2`, which are switched on according to the value of the residual in the Newton iteration described in Algorithm 3. How the value is actually computed may affect the performance of the algorithm (see e.g. [53]). For a generic residual vector \mathbf{v} of length M , here we adopt the rescaled maximum norm

$$\|\mathbf{v}\| = \max_{i=1,\dots,M} (v_i \cdot s c_i^{-1}),$$

where $s c_i := \max(s c_i, |\mathbf{w}_{k+1,i}|)$ is the local maximum of the solution vector at the k -th Newton step, and it is reinitialised as $s c_i = \max(|\mathbf{w}^n|_2, \eta)$, where $\eta = \frac{\text{ATOL}}{\text{RTOL}}$. This process is summarised in Line 1 from Algorithm 2.

We recall (see Line 1 of Algorithm 3) that the residual in the Newton step is simply the norm of the current increment $\delta_{k+1} \mathbf{w}_z^*$. The loop can break under different cases. For instance, if the residual is smaller than a given threshold, then Line 2 terminates the step. Otherwise, the linear convergence of the overall scheme (see e.g. [25]) implies that one can evaluate the iteration error using the residual together with the inequality $\|\delta_{k+1} \mathbf{w}_z^*\| \leq \theta \|\delta_k \mathbf{w}_z^*\|$, with $\theta < 1$. This experimental rate is reset to zero at each mass-stiffness assembly so that it depends on the Newton iteration matrix. The rate is then estimated using $\frac{\theta}{1-\theta} \text{res}$ (see Line 20) with two successive iterations and the current error. We consider that the algorithm has converged if the error is smaller than κ_N times a fixed tolerance. A given stage is therefore rejected if at least one of the following situations occurs: (a) the convergence rate is larger than 1 (cf. Line 16); (b) the maximum number of iterations

Algorithm 2 Adaptive Runge–Kutta time stepping: **procedure** TR-BDF2(\mathbf{w}^n , \mathbf{w}_z^n , Δt , $\beta_{\Delta t}$).

```

1: compute  $sc_i = \max(|\mathbf{w}^n|_2, \eta)$ 
2: assemble  $\mathbf{M}$  and  $\mathbf{J}$  using MJCONTROL( $\mathbf{w}^n$ ,  $\mathbf{w}_z^n$ ,  $\Delta t$ ,  $\beta_{\Delta t}$ ) ▷ See Algorithm 4
3: set  $t_{n+\gamma} = t + 2\gamma\Delta t$ ,  $\mathbf{w}_0^{n+\gamma} = \mathbf{w}^n + 2\gamma\mathbf{w}_z^n$ ,  $\mathbf{w}_{z,0}^{n+\gamma} = \mathbf{w}_z^n$  ▷ Stage 2
4: rejectS1  $\leftarrow \text{false}$ 
5: set  $\text{res}_{S2,\min} = 100\epsilon \|\mathbf{w}_0^{n+\gamma}\|$ 
6: for  $k = 0, \dots, K$  do
7:   for  $* \in \{D, E\}$  do
8:      $\mathbf{g}_k^{*,n+\gamma} = -\frac{1}{\Delta t} \mathbf{M}^* \mathbf{w}_{z,k}^{*,n+\gamma} + [-\mathbf{D}^* \mathbf{w}_k^{*,n+\gamma} + \mathbf{G}^*(\mathbf{w}_k^{*,n+\gamma}) - \mathbf{C}_u^{*,n} \mathbf{w}_k^{*,n+\gamma}]$ 
9:     if  $\neg \text{mjcontrol}$  then
10:      Update  $\mathbf{M}^* = \mathbf{M}_k^{*,n+\gamma}$  and  $\mathbf{J}^* = \mathbf{J}_k^{*,n+\gamma}$ 
11:    end if
12:    solve  $\delta_{k+1}^{n+\gamma} \mathbf{w}_z^* = (\frac{1}{\Delta t} \mathbf{M}^* - \gamma \mathbf{J}^*)^{-1} \mathbf{g}_k^{*,n+\gamma}$ 
13:    compute  $\mathbf{w}_{z,k+1}^{*,n+\gamma} = \mathbf{w}_{z,k}^{*,n+\gamma} + \delta_{k+1}^{n+\gamma} \mathbf{w}_z^*$ ,  $\mathbf{w}_{k+1}^{*,n+\gamma} = \mathbf{w}_k^{*,n+\gamma} + \gamma \delta_{k+1}^{n+\gamma} \mathbf{w}_z^*$ 
14:    update Robin transmission conditions  $\mathcal{R}_h^*$  from (2.7)
15:   end for
16:   NEWTONCONV( $\mathbf{w}_{k+1}^{n+\gamma}$ ,  $\delta_{k+1}^{n+\gamma} \mathbf{w}_z$ ,  $\text{res}_{S2,\min}$ ,  $\beta_{\Delta t}$ ) ▷ See Algorithm 3
17: end for
18: rejectS2  $\leftarrow \text{false}$ 
19: if  $\neg \text{rejectS1}$  then ▷ Stage 3
20:   compute  $sc_i = \max(|\mathbf{w}^{n+\gamma}|_2, sc_i)$ 
21:    $\mathbf{w}_{z,0}^{\text{new}} = p_{31} \mathbf{w}_z^n + p_{32} \mathbf{w}_z^{n+\gamma} + p_{33} \mathbf{w}^{n+\gamma} - p_{33} \mathbf{w}^n$ 
22:    $\mathbf{w}_0^{\text{new}} = \mathbf{w}^n + (1 - b_2 - \gamma) \mathbf{w}_z^n + b_2 \mathbf{w}_z^{n+\gamma} + \gamma \mathbf{w}_{z,0}^{\text{new}}$ 
23:   redo steps 6–15 to retrieve  $\mathbf{w}_{z,k+1}^{\text{new}}$  and  $\mathbf{w}_{k+1}^{\text{new}}$ 
24: end if
25: if  $\text{rejectS1} \vee \text{rejectS2}$  then
26:   if  $\text{mjcontrol}$  then
27:     if  $J_{\text{current}} \wedge M_{\text{current}}$  then
28:       set  $\Delta t^{\text{old}} = \Delta t$ ,  $\Delta t = \max(fac_{S1S2} \Delta t^{\text{old}}, \Delta t^{\text{min}})$ ,  $\mathbf{w}_z^n = \frac{\Delta t}{\Delta t^{\text{old}}} \mathbf{w}_z^n$ 
29:       needNewMJ  $\leftarrow \text{true}$ 
30:     else
31:       needNewJ  $\leftarrow \neg J_{\text{current}}$ , needNewM  $\leftarrow \neg M_{\text{current}}$ 
32:     end if
33:   else
34:     set  $\Delta t^{\text{old}} = \Delta t$ ,  $\Delta t = \max(fac_{S1S2} \Delta t^{\text{old}}, \Delta t^{\text{min}})$ ,  $\mathbf{w}_z^n = \frac{\Delta t}{\Delta t^{\text{old}}} \mathbf{w}_z^n$ 
35:   end if
36: else
37:   compute  $sc_i = \max(|\mathbf{w}^{\text{new}}|_2, sc_i)$ 
38:    $\mathbf{e}_w^1 = (\hat{b}_1 - b_1) \mathbf{w}_z^n + (\hat{b}_2 - b_2) \mathbf{w}_z^{n+\gamma} + (\hat{b}_3 - b_3) \mathbf{w}_z^{n+1}$ 
39:   if  $\neg \text{mjcontrol}$  then
40:     Update  $\mathbf{M} = \mathbf{M}^{\text{new}}$  and  $\mathbf{J} = \mathbf{J}^{\text{new}}$ 
41:   end if
42:   compute  $\mathbf{e}_w^2 = (\frac{1}{\Delta t} \mathbf{M} - \gamma \mathbf{J})^{-1} \mathbf{e}_w^1$  and  $\text{err} = \max(\|\mathbf{e}_w^2\|, \frac{\|\mathbf{e}_w^1\|}{16})$ 
43:   if  $\text{err} > R_{\text{TOL}}$  then
44:      $\Delta t^{\text{old}} = \Delta t$ ,  $\Delta t = \max\left(\Delta t^{\text{old}} \max\left(fac_{\text{min}}, fac\left(\frac{R_{\text{TOL}}}{\text{err}}\right)^{k_I}\right), \Delta t^{\text{min}}\right)$ ,  $\mathbf{w}_z^n = \frac{\Delta t}{\Delta t^{\text{old}}} \mathbf{w}_z^n$ 
45:     needNewMJ  $\leftarrow \text{true}$ 
46:   end if
47: end if

```

$K = 10$ is reached (cf. [25] and Line 23); and (c) For any k , we have $\kappa_N TOL_N < e(\delta_{k+1} \mathbf{w}_z, \widehat{\mathbf{c}}) \theta^{K-k}$ (cf. Line 26). Point (c) represents a rough estimate of the iteration error expected after $K - 1$ iterations.

Should a stage be rejected, one moves to Line 25 in Algorithm 2 and reduces the timestep Δt by a factor fac_{S1S2} (independently of the mass matrix assembly). Then, Line 31 checks whether both mass and Jacobian matrices have been updated. Finally, Line 36 verifies that the local error estimation remains below a prescribed tolerance. Based on the estimators for the scaled derivatives we proceed to compute the local asymptotic error \mathbf{e}_w^1 as a result from the linear system stated in Line 42 of Algorithm 2. This step is necessary as the boundedness of the raw estimator is not always guaranteed [25].

Next, we select the maximum error between these two estimators as an approximation of the timestep error. In contrast with [25], we do not observe here the so-called *hump* phenomenon intrinsic to automatic step methods, so we do not require an additional correction step. We only update the timestep in an automatic fashion (thanks to the sequence of rejection procedures), capturing correctly the dynamics of the integrated system. When all errors are lower than the corresponding tolerance, the timestep is accepted and the interface elasticity problem is solved in Line 11 from Algorithm 1. We stress that the algorithm will stop if $\Delta t \leq \Delta t^{\text{min}}$.

Algorithm 4 permits to control the mass-stiffness assembly. This procedure consists of a number of controllers, including the aforementioned mjcontrol (see a list in Table 3.2). The state modification of these variables depends on step-size revaluation, which itself depends on the rejected stage of the RK method. Notice that M_{current} and J_{current} control whether the mass and Jacobian matrices are evaluated at each new timestep (if this timestep is rejected at least once). For

Algorithm 3 Newton stopping criterion: **procedure** NEWTONCONV(\mathbf{w}_{k+1} , $\delta_{k+1}\mathbf{w}_z$, res_{\min} , $\beta_{\Delta t}$).

```

1: compute  $\widehat{s}_c = \max(s_c, |\mathbf{w}_{k+1,i}|)$  and  $\text{res}_{k+1}(\widehat{s}_c) = \|\delta_{k+1}\mathbf{w}_z\|$ 
2: if  $\text{res}_{k+1} \leq \text{res}_{\min}$  then
3:   break
4: else if  $k = 0$  then
5:   if needNewRate  $\wedge$  Stage 2 then
6:     if mjcontrol then
7:       needNewRate  $\leftarrow$  false
8:     end if
9:    $\theta = 0$ 
10:  else
11:     $e(\delta_{k+1}\mathbf{w}_z, \widehat{s}_c) = \frac{\theta}{1-\theta} \text{res}_{k+1}$ 
12:    if  $e(\delta_{k+1}\mathbf{w}_z, \widehat{s}_c) \leq 0.1\kappa_N \text{TOL}_N$  then
13:      break
14:    end if
15:  end if
16: else if  $\text{res}_{k+1} > 0.9\text{res}_k$  then                                 $\triangleright$  Divergence
17:   rejectSX  $\leftarrow$  true
18:   break
19: else
20:   set  $\theta = \max(0.9\theta, \frac{\text{res}_{k+1}}{\text{res}_k})$  and  $e(\delta_{k+1}\mathbf{w}_z, \widehat{s}_c) = \frac{\theta}{1-\theta} \text{res}_{k+1}$ 
21:   if  $e(\delta_{k+1}\mathbf{w}_z, \widehat{s}_c) \leq \kappa_N \text{TOL}_N$  then                                 $\triangleright$  Convergence
22:     break
23:   else if  $k = K$  then                                          $\triangleright$  Max. iterations attained
24:     rejectSX  $\leftarrow$  true
25:     break
26:   else if  $\kappa_N \text{TOL}_N < e(\delta_{k+1}\mathbf{w}_z, \widehat{s}_c)\theta^{K-k}$  then           $\triangleright$  Divergence
27:     rejectSX  $\leftarrow$  true
28:     break
29:   end if
30: end if

```

Algorithm 4 Control of mass-stiffness assembly: **procedure** MJCONTROL(\mathbf{w}^n , \mathbf{w}_z^n , Δt , $\beta_{\Delta t}$).

```

1: if needNewM  $\wedge$  mjcontrol then
2:   compute  $\mathbf{M}^{*,n}$ , with  $* \in \{D, E\}$ 
3:   Mcurrent  $\leftarrow$  true, needNewM  $\leftarrow$  false, needNewMJ  $\leftarrow$  true
4: end if
5: if needNewJ  $\wedge$  mjcontrol then
6:   compute  $\mathbf{J}^{*,n} = -\mathbf{D}^* + \mathbf{J}_{G^*}^n - \mathbf{C}_u^{*,n}$  with  $* \in \{D, E\}$ 
7:   Jcurrent  $\leftarrow$  true, needNewJ  $\leftarrow$  false, needNewMJ  $\leftarrow$  true
8: end if
9: if needNewMJ  $\wedge$  mjcontrol then
10:  compute  $\frac{1}{\Delta t} \mathbf{M}^{*,n} - \gamma \mathbf{J}^{*,n}$  with  $* \in \{D, E\}$ 
11:  needNewMJ  $\leftarrow$  false, needNewRate  $\leftarrow$  true
12: end if

```

Table 3.2

Set of Booleans controlling the evaluation and assembly of mass and stiffness matrices.

| | |
|-----------|---|
| mjcontrol | Switch to reuse Newton iteration matrices over two implicit stages |
| needNewM | Need to evaluate mass matrix \mathbf{M}^* |
| needNewJ | Need to evaluate Jacobian matrix \mathbf{J}^* |
| needNewMJ | Need to evaluate mass-Jacobian matrix $\frac{1}{\Delta t} \mathbf{M}^* - \gamma \mathbf{J}^*$ |
| Mcurrent | Appropriate mass matrix \mathbf{M} for the current timestep |
| Jcurrent | Appropriate Jacobian matrix \mathbf{J} for the current timestep |

models such as (2.2), the label `Mcurrent` is always **true**. However if we want to solve the interface problem using e.g. a level-set approach, then the mass matrix needs to be recomputed and the controller can be exploited.

4. Numerical tests

This section contains a set of examples assessing the experimental spatio-temporal convergence of our primal-mixed method, and also illustrates its use in two mechanochemical interface problems. The implementation is carried out with the open-source finite element library FreeFem++ [17], and all sparse linear systems are solved with distributed direct methods (MUMPS and UMFPACK).

Example 1: Experimental accuracy against manufactured solutions. Let us consider a rectangular domain $\Omega = (0, 1) \times (0, 1.4)$ divided into the dermis $\Omega^D = (0, 1)^2$ and epidermis $\Omega^E = \Omega \setminus \Omega^D$ subdomains. The initial position of the interface is characterised by the segment $x \in (0, 1)$, $y = 1$, and the external surface is $x \in (0, 1)$, $y = 1.4$. The main goal of our first

series of tests is to analyse the convergence of the spatial discretisation. We therefore focus on a stationary problem where no advection occurs in the morphogen model. We construct smooth exact solutions, defined as follows:

$$\tilde{\mathbf{w}} = \begin{pmatrix} 1 - \cos(2\pi x) \sin(3\pi y) \\ 1 + \frac{1}{2} \cos(2\pi x) \sin(3\pi y) \end{pmatrix}, \quad \tilde{\mathbf{u}} = \begin{pmatrix} x(1-x) \cos(\pi x) \sin(2\pi y) \\ \sin(\pi x) \cos(\pi y) y^2(1-y) \end{pmatrix}, \quad (4.1)$$

and set $\mathbf{u}^D = \tilde{\mathbf{u}}|_{\Omega^D}$, $\mathbf{u}^E = \tilde{\mathbf{u}}|_{\Omega^E}$, $\mathbf{w}^D = \tilde{\mathbf{w}}|_{\Omega^D}$, $\mathbf{w}^E = \tilde{\mathbf{w}}|_{\Omega^E}$, and $p^* = -\lambda^* \operatorname{div} \tilde{\mathbf{u}}^*$. The functions in (4.1) are used to construct the Dirichlet datum for the displacements on $\partial\Omega \setminus \Gamma$ as well as the flux conditions imposed on the morphogens at the boundary $\partial\Omega$. Suitable non-homogeneous forcing terms are also set using these closed-form solutions. We choose the two-species Gierer–Meinhardt reaction model (2.3), and adopt the coupling terms as in (2.5). Model parameters are chosen as in Table 4.1.

We proceed to generate a sequence of successively refined unstructured triangular meshes for both subdomains, and compute errors between exact and approximate numerical solutions (recall that we are solving for the steady version of the coupled problem) on each refinement level. For a generic scalar or vector field s^* we will denote errors and convergence rates as follows

Table 4.1

Example 1. Parameters for the mechanochemical model using (2.3) and (2.5).

| | | | | | | |
|---------------|---------------|---|----------------|-------------------|-------------------|-----------------|
| $c_f^D = 150$ | $c_g^D = 1$ | $\rho_0^D = \rho_2^D = \rho_3^D = \rho_5^D = 1$ | $\rho_1^D = 0$ | $\rho_4^D = 0.35$ | $M_{11}^D = 1$ | $M_{22}^D = 30$ |
| $c_f^E = 20$ | $c_g^E = 2$ | $\rho_0^E = \rho_2^E = \rho_3^E = 2$ | $\rho_5^E = 1$ | $\rho_1^E = 0$ | $\rho_4^E = 0.15$ | $M_{11}^E = 2$ |
| $E^D = 1000$ | $v^D = 0.475$ | $J^D = 1$ | $K^D = 1e5$ | $E^E = 10$ | $v^D = 0.33$ | $J^E = 1$ |

Table 4.2

Example 1. Spatial and temporal error history associated to the discretisation of the model problem. Errors on the bottom sub-table were obtained on a fine mesh of size $h = 0.0013$, and computed until a final time $T = 0.02$.

| Space convergence | | | | | | | | | |
|-------------------|------------------------------|------------------------------|------------------------------|------------------------------|---------------------|---------------------|---------------------|---------------------|---------------------|
| DoF | h | $e_1(\mathbf{w}^D)$ | $r_1(\mathbf{w}^D)$ | $e_1(\mathbf{w}^E)$ | $r_1(\mathbf{w}^E)$ | $e_0(p^D)$ | $r_0(p^D)$ | $e_0(p^E)$ | $r_0(p^E)$ |
| 48 | 0.5207 | 5.6275 | – | 3.5698 | – | 1175.8 | – | 2.2114 | – |
| 108 | 0.2828 | 4.1858 | 0.5794 | 2.6495 | 0.4886 | 44412 | 1.9061 | 1.2433 | 0.9437 |
| 280 | 0.1736 | 2.6223 | 0.7956 | 1.8701 | 0.7133 | 129.18 | 2.1008 | 0.6340 | 1.3790 |
| 900 | 0.0889 | 1.4380 | 0.9447 | 0.9974 | 0.9398 | 37.750 | 1.9344 | 0.2178 | 1.5973 |
| 3264 | 0.0432 | 0.7485 | 0.9844 | 0.4852 | 0.9978 | 11.335 | 1.8138 | 0.0801 | 1.3849 |
| 12276 | 0.0218 | 0.3829 | 0.9890 | 0.2480 | 0.9788 | 3.6282 | 1.6805 | 0.0409 | 0.9624 |
| 47320 | 0.0110 | 0.1970 | 0.9695 | 0.1326 | 0.9217 | 1.4185 | 1.3701 | 0.0252 | 0.9748 |
| 186276 | 0.0055 | 0.1065 | 0.9928 | 0.0684 | 0.9605 | 0.7001 | 0.9599 | 0.0141 | 0.9635 |
| DoF | h | $e_0(\mathbf{u}^D)$ | $r_0(\mathbf{u}^D)$ | $e_1(\mathbf{u}^D)$ | $r_1(\mathbf{u}^D)$ | $e_0(\mathbf{u}^E)$ | $r_0(\mathbf{u}^E)$ | $e_1(\mathbf{u}^E)$ | $r_1(\mathbf{u}^E)$ |
| 48 | 0.5207 | 0.0605 | – | 1.2176 | – | 0.0423 | – | 0.5038 | – |
| 108 | 0.2828 | 0.0255 | 1.6925 | 0.6149 | 1.3372 | 0.0192 | 1.2900 | 0.3408 | 0.6409 |
| 280 | 0.1736 | 0.0081 | 1.9584 | 0.2545 | 1.5009 | 0.0093 | 1.4921 | 0.2226 | 0.8723 |
| 900 | 0.0889 | 0.0024 | 1.9235 | 0.1201 | 1.1808 | 0.0029 | 1.7335 | 0.1131 | 1.0121 |
| 3264 | 0.0432 | 0.0006 | 1.9717 | 0.0596 | 1.0563 | 0.0011 | 1.2942 | 0.0537 | 1.0313 |
| 12276 | 0.0218 | 0.0002 | 1.9373 | 0.0299 | 1.0180 | 0.0006 | 1.9020 | 0.0275 | 0.9765 |
| 47320 | 0.0110 | 3.61e-5 | 1.9734 | 0.0150 | 1.0061 | 3.70e-5 | 1.9258 | 0.0151 | 0.9848 |
| 186276 | 0.0055 | 9.02e-6 | 1.8221 | 0.0075 | 1.0020 | 9.12e-6 | 1.8300 | 0.0065 | 0.9730 |
| Time convergence | | | | | | | | | |
| Δt | $e_{\Delta t}(\mathbf{w}^D)$ | $r_{\Delta t}(\mathbf{w}^D)$ | $e_{\Delta t}(\mathbf{w}^E)$ | $r_{\Delta t}(\mathbf{w}^E)$ | avg(iter) | | | | |
| 0.0100 | 0.2002 | – | 0.0881 | – | 3 | | | | |
| 0.0050 | 0.0982 | 1.1294 | 0.0292 | 1.1752 | 3 | | | | |
| 0.0025 | 0.0230 | 1.9301 | 0.0094 | 1.7388 | 3 | | | | |
| 0.0013 | 0.0056 | 1.9614 | 0.0024 | 1.7929 | 3 | | | | |
| 0.0006 | 0.0016 | 1.9811 | 0.0006 | 1.9952 | 3 | | | | |
| 0.0002 | 0.0004 | 1.9937 | 0.0002 | 1.9874 | 3 | | | | |

Table 4.3

Example 2. Adaptive timestep controller parameters.

| | | | | | |
|----------------------|---------------|----------------------|------------|------------------|------------------|
| Δt^{max} | 2000 | R _{TOL} | 10^{-6} | A _{TOL} | 10^{-3} |
| T _{OL,N} | 10^{-6} | κ_N | 0.5 | K | 10 |
| fac_{S1S2} | 0.3 | fac_{min} | 0.1 | fac | $\sqrt[3]{0.25}$ |
| ratio _{min} | 0.2 | ratio _{max} | 5.0 | ratio | $\sqrt[3]{0.25}$ |
| k_I | $\frac{1}{3}$ | ϵ | 10^{-10} | | |

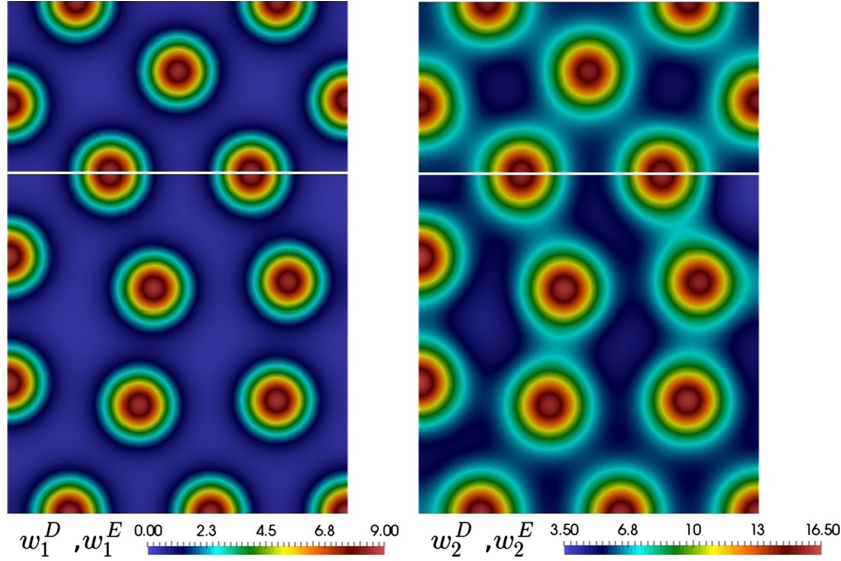


Fig. 4.1. Example 2. Species concentrations w_1^*, w_2^* computed at $T = 2000$. (For interpretation of the colours in the figure(s), the reader is referred to the web version of this article.)

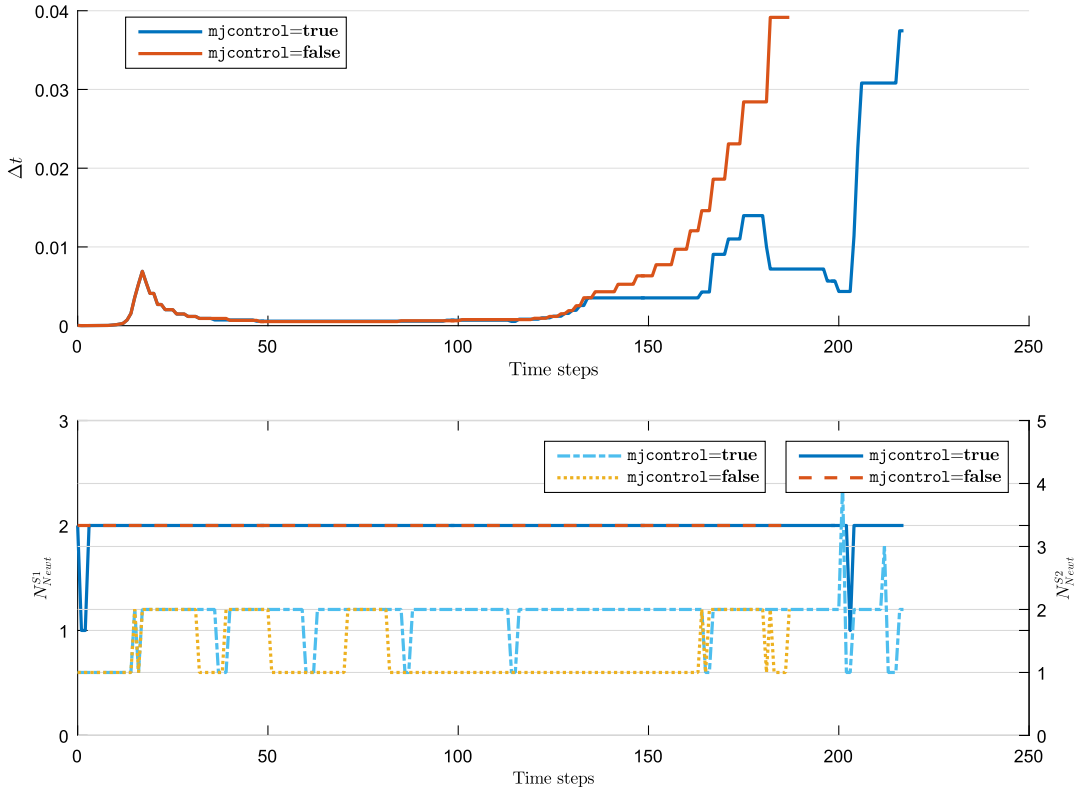


Fig. 4.2. Example 2. Time step evolution and number of Newton iterations needed to converge on stages S₁ and S₂, and setting `mjcontrol` on and off.

$$e_0(s^*) := \|s^* - s_h^*\|_{0,\Omega^*}, \quad e_1(s^*) := \|s^* - s_h^*\|_{1,\Omega^*}, \quad r_k(s^*) = \frac{\log(e_k(s^*)/\hat{e}_k(s^*))}{\log(h/\hat{h})}, \quad k = 0, 1,$$

where e_k and \hat{e}_k denote errors computed on two consecutive meshes of sizes h and \hat{h} , respectively. The outcome of the convergence test (using the MINI-element for the approximation of displacement and pressure, and Lagrangian finite elements for the species concentration) is presented in the first part of Table 4.2, which indicates that the method converges optimally (with respect to the interpolation properties of the finite element spaces). Four Newton iterations are sufficient for

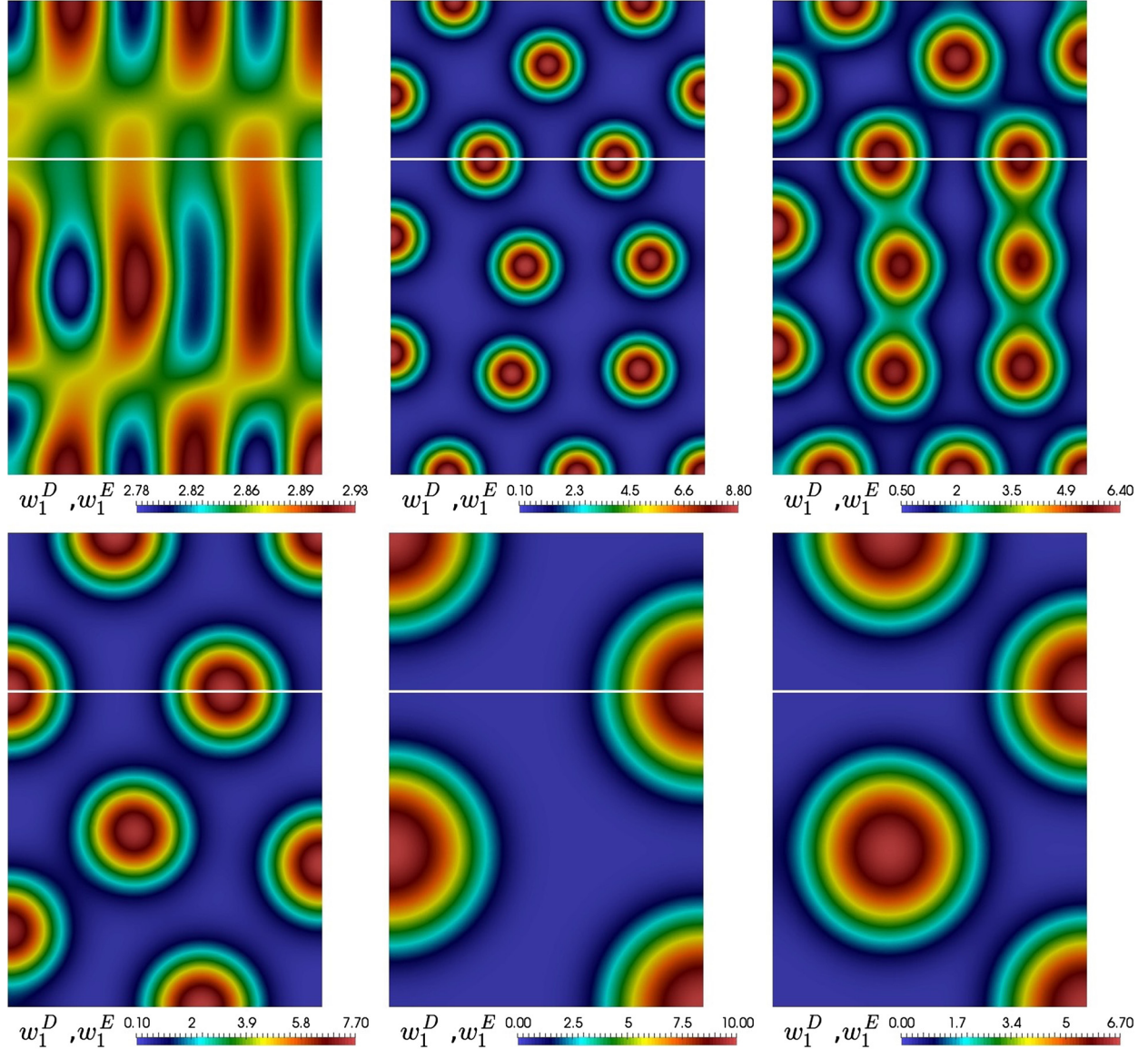


Fig. 4.3. Example 2, 2D case. Concentration of species w_1^* . Linear cross-diffusion (top row) using $(M_{12}^*, M_{21}^*) = (0.5, 0)$, $(0, 0.5)$ and $(0.35, 0.05)$ (left, centre, right, respectively). The bottom panels show the case of nonlinear cross-diffusion using $(\eta_{11}^{*,w_1}, \eta_{11}^{*,w_2}, \eta_{22}^{*,w_1}, \eta_{22}^{*,w_2}) = (10^{-1}, 10^{-1}, 10^{-1}, 10^{-1})$, $(1, 0, 0, 1)$ and $(1, 0, 1, 0)$ (left, centre, right, respectively).

each mesh to reach the tolerance of $\text{TOL}_N = 1e-5$, and the stopping criterion is based on the ℓ^∞ -norm of the total residual. The time convergence is assessed by taking a fine mesh of size $h = 0.0013$ and computing approximate solutions to the transient coupled problem (2.1), (2.2) compared against the exact displacement and pressure from (4.1) whereas the species concentrations are now

$$\mathbf{w} = \tilde{\mathbf{w}} \exp(-kt),$$

with $k = \log(1/2)$, and \mathbf{w} is as in (4.1). Errors and convergence rates are measured and denoted as follows

$$e_{\Delta t}(s^*) := \sum_{n=1}^N \|s^*(t^n) - s_h^*(t^n)\|_{0,\Omega^*}, \quad r_{\Delta t}(s^*) = \frac{\log(e_{\Delta t}(s^*)/\widehat{e}_{\Delta t}(s^*))}{\log(\Delta t/\widehat{\Delta t})},$$

where $e_{\Delta t}, \widehat{e}_{\Delta t}$ denote errors computed using two consecutive timesteps Δt and $\widehat{\Delta t}$, respectively. The second block in Table 4.2 shows an asymptotic second order convergence, as expected from the use of the TR-BDF2 time stepping algorithm (see also [9,16]).

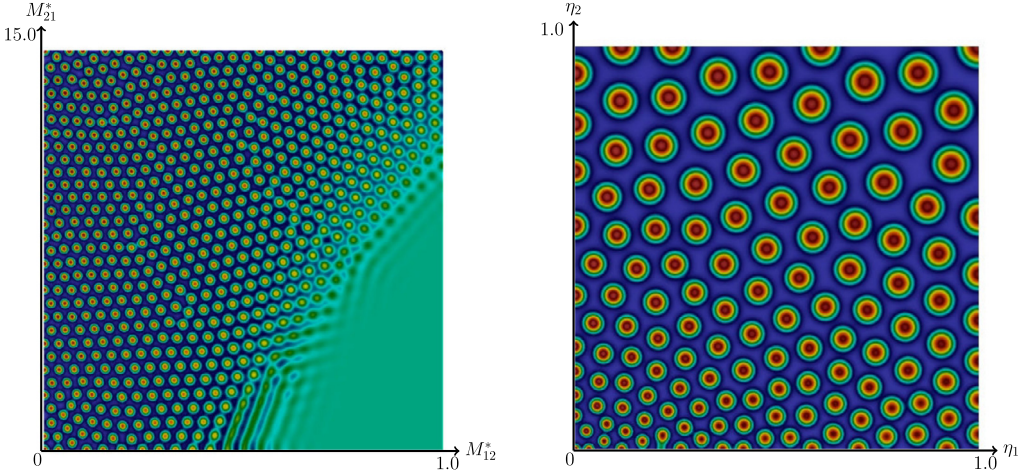


Fig. 4.4. Example 2. Space parameter plots produced with linear (left) and nonlinear (right) cross-diffusion terms.

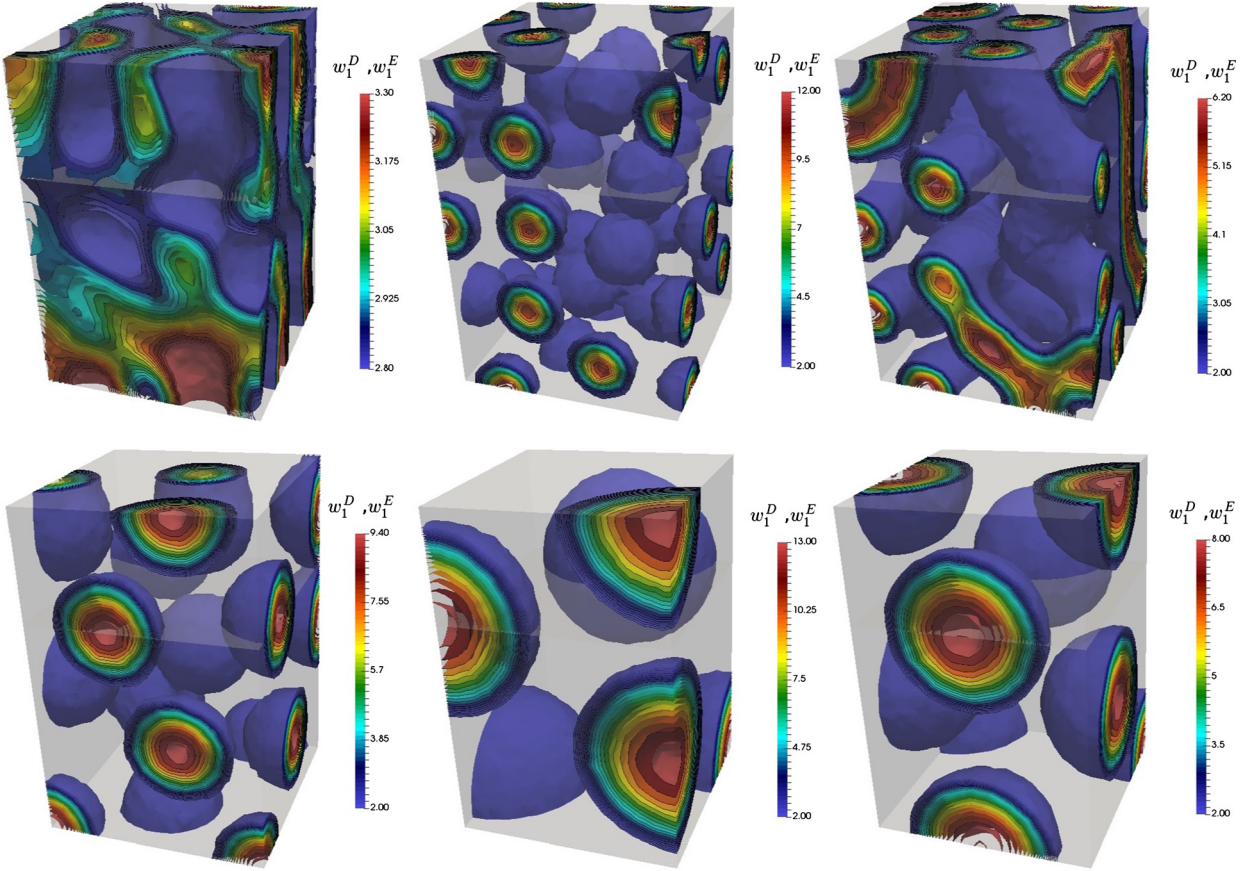


Fig. 4.5. Example 2, 3D case. Concentration of species w_1^* . Linear cross-diffusion (top row) using $(M_{11}^*, M_{21}^*) = (0.5, 0)$, $(0, 0.5)$ and $(0.35, 0.05)$ (left, centre, right, respectively). The bottom panels show the case of nonlinear cross-diffusion using $(\eta_{11}^{*,w_1}, \eta_{11}^{*,w_2}, \eta_{22}^{*,w_1}, \eta_{22}^{*,w_2}) = (10^{-1}, 10^{-1}, 10^{-1}, 10^{-1})$, $(1, 0, 0, 1)$ and $(1, 0, 1, 0)$ (left, centre, right, respectively).

Example 2: Cross-diffusion effects in a two-dimensional morphogen interface model. In this example we focus our attention on the effect of cross-diffusion $M_{ij}^* \neq 0 \forall i, j$ in (2.2). We consider again the Gierer-Meinhardt kinetics (2.3), now decoupled from the linear elasticity equations (2.1). We impose the same reaction parameters on both sides of the interface $\rho_0 = 0$, $\rho_1 = \rho_2 = \rho_4 = \rho_5 = 1$, $\rho_3 = 0.35$, we set the diffusion coefficients $M_{11} = M_1 = 1$, $M_{22} = M_2 = 30$, and choose the acceleration transmission constants $K^D = K^E = 1$. The domains of interest are the blocks $\Omega^D = (0, 50)^2$ and

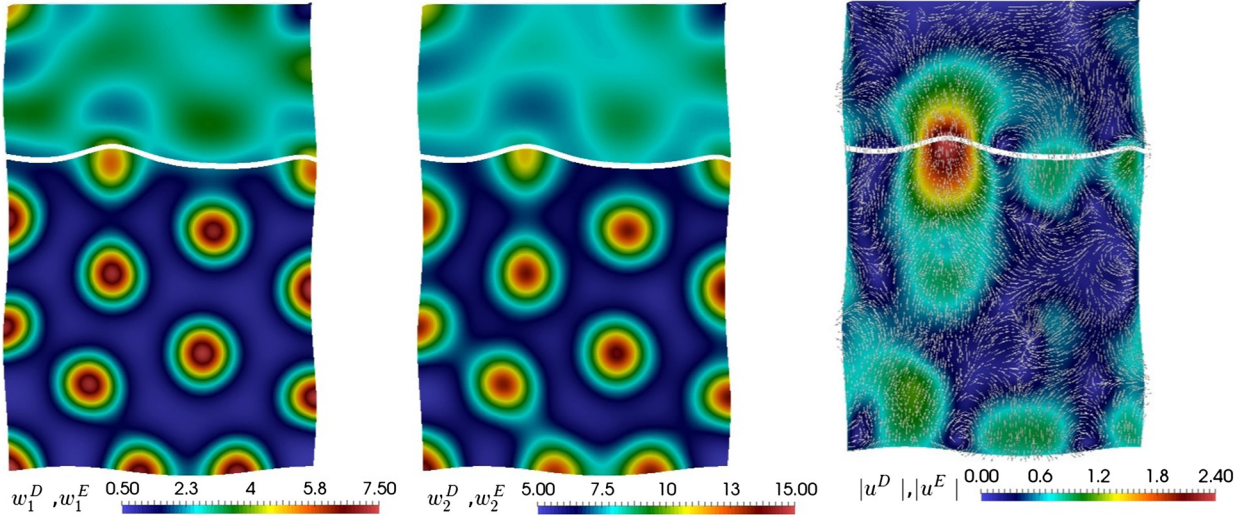


Fig. 4.6. Example 3. Morphogen concentrations w_1^* , w_2^* (left and centre) and displacement magnitude (right), computed at $T = 2000$ and plotted on the deformed configuration.

Table 4.4

Example 4. Parameters for the mechanochemical model using (2.4) and (2.5).

$$\begin{aligned} c_f^D &= 20, c_g^D = 1, r_1 = 0.25, r_0 = 1, r_2 = 20, r_3 = 5, r_4 = 5, M_{11}^D = M_{22}^D = 1, M_{33}^D = 35, M_{44}^D = 10, \\ c_f^E &= 20, c_g^E = 1, r_5 = 5.0, r_6 = 20.0, r_7 = 5.0, M_{11}^E = M_{22}^E = 1, M_{33}^E = 35, M_{44}^E = 10, \\ E^* &= 1000, \nu^* = 0.475, J^* = K^* = 1, \alpha^E = 9.5 \end{aligned}$$

$\Omega^E = (0, 50) \times (50, 75)$, which we discretise into unstructured meshes with 16360 and 8032 triangular elements, respectively. Initial concentrations are set according to

$$\tilde{w}_1 = \frac{\rho_2}{\rho_3} \left(\rho_0 + \rho_1 \frac{\rho_5}{\rho_4} \right), \quad \tilde{w}_2 = \frac{\rho_4}{\rho_5} \tilde{w}_1^2, \quad \mathbf{w}_0^*(\mathbf{x}) = \begin{pmatrix} \tilde{w}_1(1 + \eta(\mathbf{x})) \\ \tilde{w}_2 \end{pmatrix},$$

where $\eta(\mathbf{x})$ is a uniformly distributed random field with variance 10^{-3} . We employ the adaptive time-stepping method described in Algorithm 2 with controller parameters defined as in Table 4.3. We simulate the process until $T = 2000$, and display the resulting numerical solutions on Fig. 4.1.

In Fig. 4.2 we observe that the adaptive time stepping behaves differently depending on whether one reuses or not the Newton iteration matrices over the implicit stages (this feature is turned on/off by the parameter `mjcontrol`). For each case, we observe an increase of Δt as the system reaches a steady state. The spatial patterns generated by the two approaches practically coincide and therefore are not shown. However, we observe that the case `mjcontrol = true` does not show a marked increase of the timestep when the system reaches stationary patterns. Additionally, we observe that reusing the iteration matrix leads to a slight increase in the number of Newton iterations in the S2 stage.

In addition, we test our algorithm for both linear and nonlinear cross-diffusion terms defined as

$$\mathbf{M}_{lin}^*(\mathbf{w}^*) = \begin{pmatrix} M_{11}^* & M_{12}^* \\ M_{21}^* & M_{22}^* \end{pmatrix}$$

or

$$\mathbf{M}_{nl}^*(\mathbf{w}^*) = \begin{pmatrix} M_{11}^*(1 + \eta_{11}^{*,w_1} w_1^* + \eta_{11}^{*,w_2} w_2^*) & 0 \\ 0 & M_{22}^*(1 + \eta_{22}^{*,w_1} w_1^* + \eta_{22}^{*,w_2} w_2^*) \end{pmatrix},$$

where M_{ij}^* , η_{ij}^{*,w_k} ($i, j, k = \{1, 2\}$) are real constants. For these simulations we impose $M_{11}^* = M_1^*$, $M_{22}^* = M_2^*$. As illustrated in Fig. 4.3, the final patterns adopt different structures according to the cross-diffusion matrix employed. While the specific nonlinear cross-diffusion matrix modifies the size of w_i -concentration spots without changing its structure, the linear one (and depending on the parameter values) can change from spots to striped patterns. Furthermore, nonlinear cross-diffusion induces a more visible impact on the distance between high concentration regions, when compared to the linear case. Space-parameter plots illustrate this phenomenon in Fig. 4.4. For both cross-diffusion models, we vary spatially the values $[M_{12}^*, M_{21}^*] \in [0, 1] \times [0, 15]$, and $\eta_{11}^{*,w_1} = \eta_{22}^{*,w_1} = \eta_1$ and $\eta_{11}^{*,w_2} = \eta_{22}^{*,w_2} = \eta_2$ from 0 to 1; always checking that the cross-diffusion matrices remain positive definite. The linear cross-diffusion particularly affects the type of patterns that are

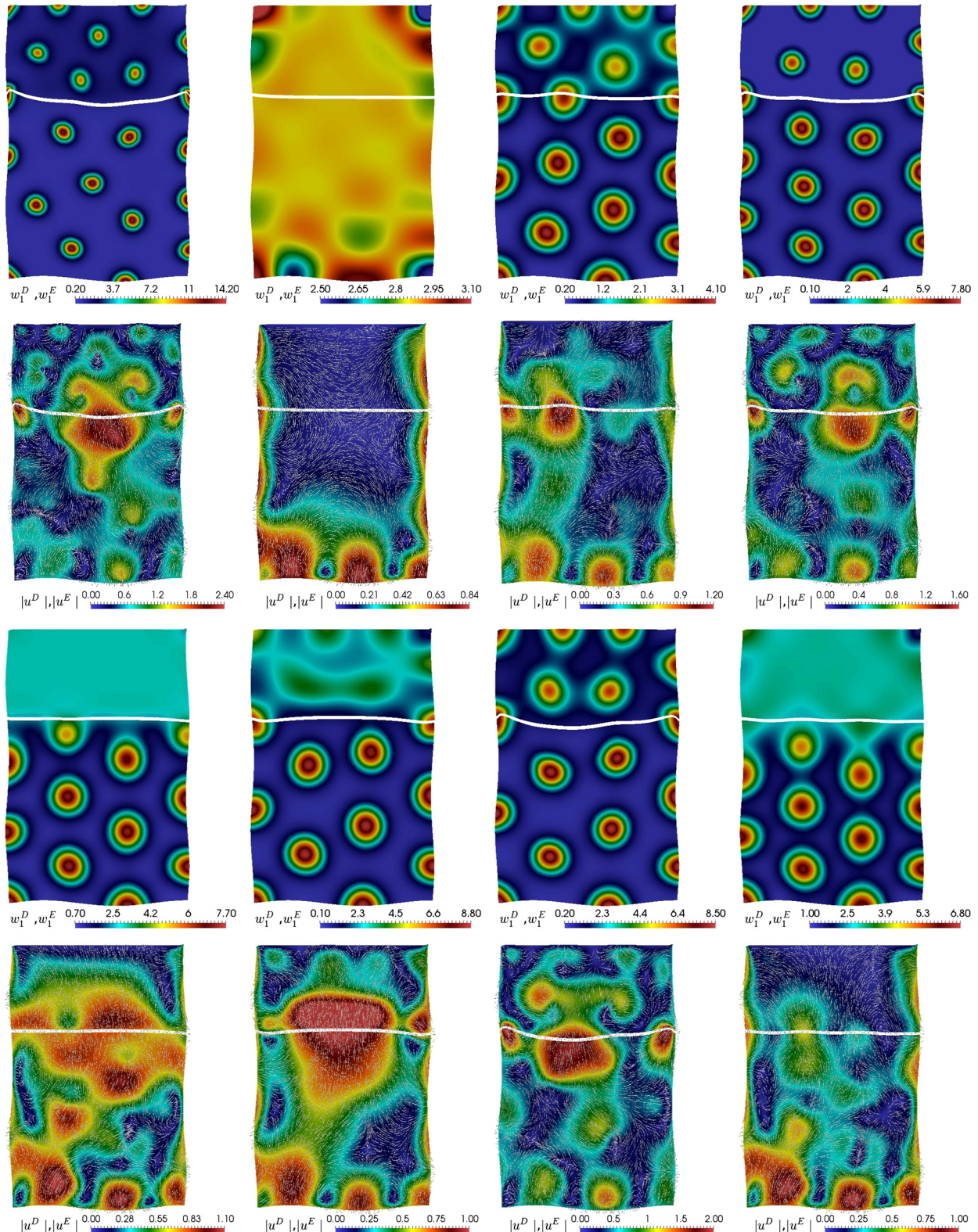


Fig. 4.7. Example 3. Concentration of species w_1^* and displacement magnitude $|u^*|$. Influence of ADR parameters (1st & 2nd rows) using $M_1^* = 0.5$, $M_1^* = 1.5$, $\rho_2^* = 0.5$ and $\rho_3^* = 0.45$ (from left to right respectively); and of coupling parameters (3rd & 4th rows) using $c_f^* = 150$, $c_f^* = 20$, $c_g^* = 0.5$, $c_g^* = 1.5$ (from left to right respectively).

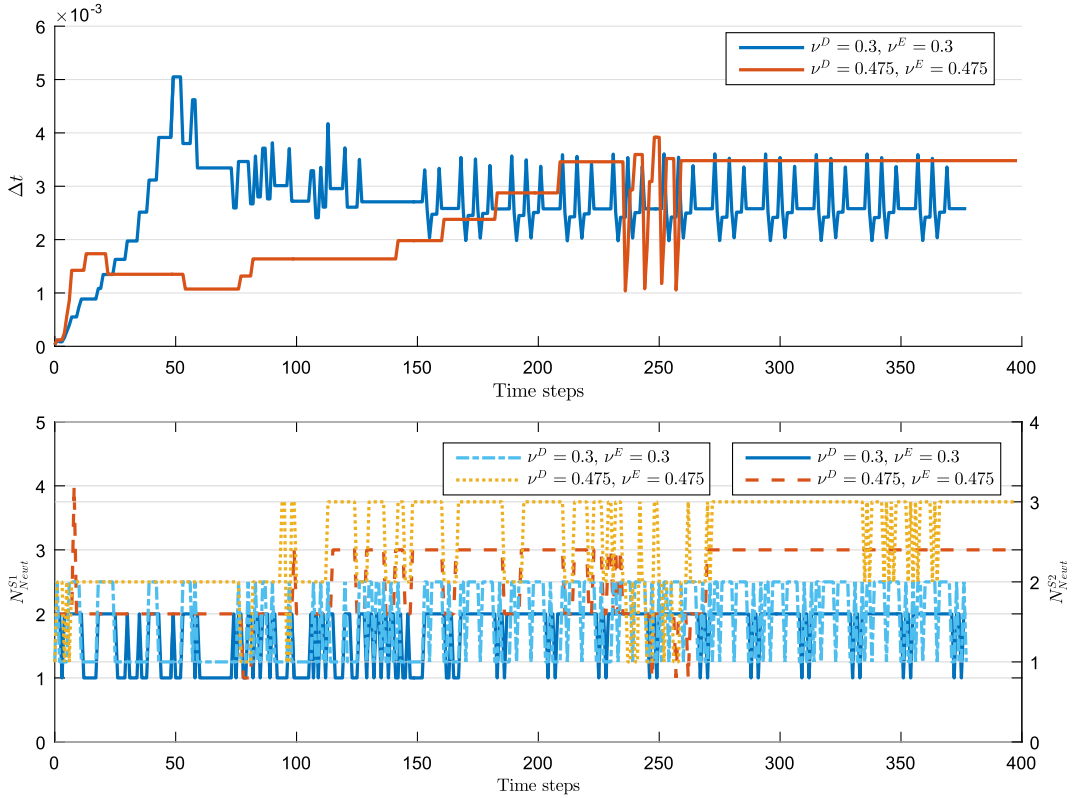


Fig. 4.8. Example 3. Timestep evolution and Newton iteration count at stages S1 and S2 for different mechanical properties.

generated but does not significantly change length scale of the pattern. Nonlinear diffusion, on the other hand, affects directly the pattern length scale without altering the general pattern structure produced by the system. These observations are confirmed in 3D domains as well (cf. 4.5).

Example 3: A simplified activator-inhibitor model on an elastic 2D domain. With the objective of testing the time-adaptive algorithms now applied to the mechanochemical coupled problem, we add the elasticity components to the reaction kinetics (2.3) of Example 2 (with the same parameters and mesh). The Young moduli and Poisson ratios defining the material properties of the medium are now $E^D = 1000$, $E^E = 250$, $\nu^D = 0.475$, $\nu^E = 0.3$. Displacements are prescribed on the boundary $\partial\Omega \setminus \Gamma$ according to $\mathbf{u} = (\frac{1}{2} \cos(5\pi(x - y)/2), \frac{3}{4} \sin(5\pi(x + y)/2))^T$. Additionally, we impose $c_f^D = 150$, $c_f^E = 20$ and $c_g^* = 1$. The medium is initially at rest and stress-free (zero displacement and pressure on the whole domain) and we re-use the initial conditions of the morphogen concentrations defined in the previous test. We use Algorithm 2 with controller parameters defined again as in Table 4.3, except for $A_{\text{TOL}} = 10^{-6}$ and $\text{TOL}_N = R_{\text{TOL}} = 10^{-4}$. The process is simulated until $T = 2000$.

Fig. 4.6 presents the final patterns generated by the morphogen concentrations and also the zones of high displacement. On the bottom layer the pattern is similar to the one in Fig. 4.1 (in terms of magnitude and spatial structure). For the layer with smaller Poisson ratio, the patterns tend to homogenise and eventually disappear. This phenomenon highlights the effects of mechanical properties on the morphogen dynamics, and we also note that deformations are larger near the interface and close to the bottom boundary of Ω^D .

We next test the influence of the reaction and mechanical coupling parameters (c_f^*, c_g^*) on the final pattern, and typical results are depicted in Fig. 4.7. Perturbations of the ADR coefficients are responsible for considerable variations on the species concentration spatial distribution as well as on the deformation profiles produced by the model. For instance, we observe that the size and shape of morphogens concentration patterns induce differences on the deformation of the interface Σ . Conversely, differences on the mechanical response of each subdomain also directly impact on the chemical species distribution, at the interface. Surprisingly, varying the coupling parameters does not substantially impact the length scale but rather make these patterns to disappear altogether.

We also inspected the effect of the acceleration constants of the ADR interface conditions together with the degree of material heterogeneity (how different the Lamé parameters are in each subdomain) on the timestep evolution and on the Newton iteration count. For these simulations we fix `mjcontrol = true` in order to inspect also the efficiency on the update of the Jacobian matrix throughout the simulation. Some of these results are collected in Figs. 4.8, 4.9, 4.10. The value N_{Newt}^{SX} represents the number of iterations corresponding to accepted timesteps. For this case we observe that Δt is

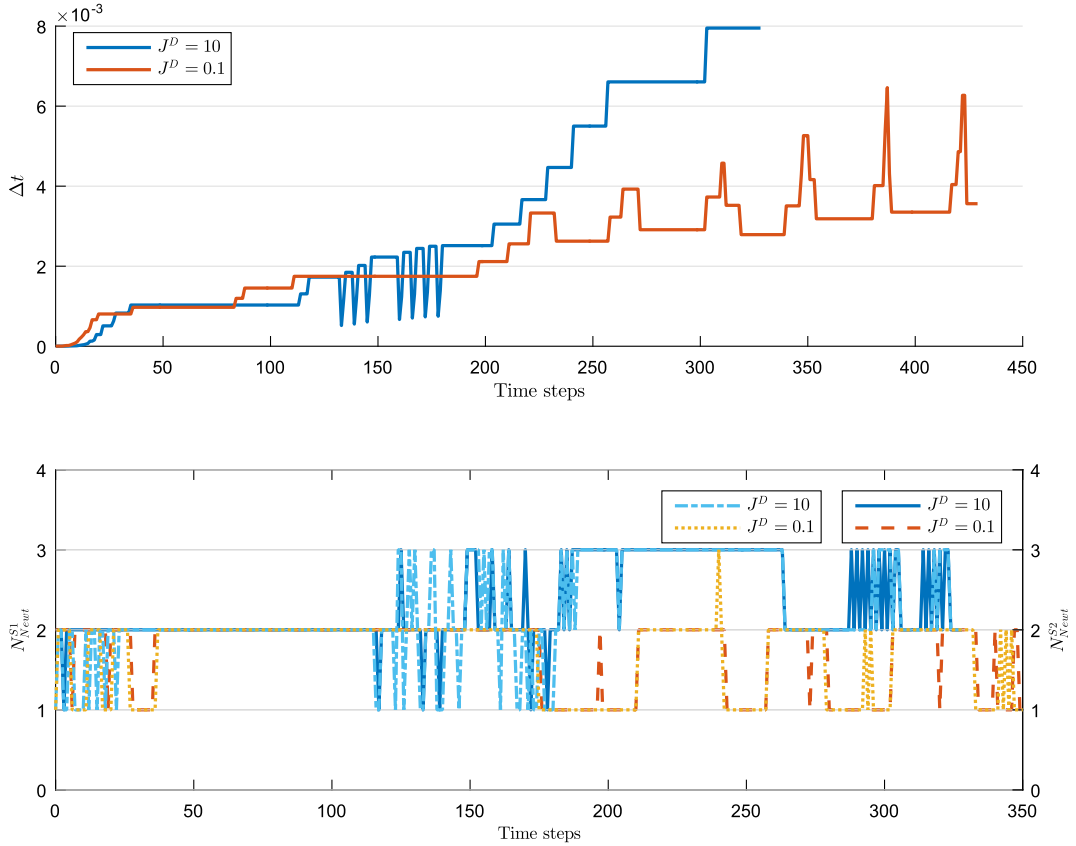


Fig. 4.9. Example 3. Timestep evolution and Newton iteration count at stages S1 and S2 for different acceleration constants.

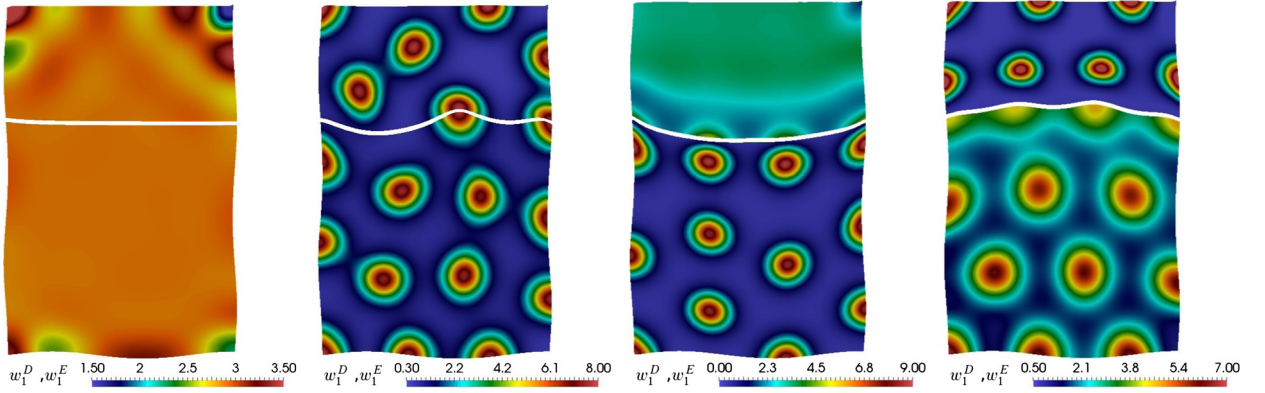


Fig. 4.10. Example 3. Species concentration w_1^* using $v^* = 0.3$, $v^* = 0.475$, $J^D = 10$ and $J^D = 0.1$ (from left to right, respectively).

of the order of 10^{-3} and progressively increases with the simulation time and the consolidation of the spatial patterns. The algorithm readily detects when the process approaches a steady state, leading to a fast increase of the timestep. However, as shown in the case using $v^* = 0.3$, this behaviour depends on the choice of model parameters and oscillations might appear, indicating a suboptimal adaptive time stepping. Moreover, changing the value of the acceleration constants may also affect the simulation time, the deformed interface, and the pattern structures. In all our experiments, we observe that accepted steps converge in less than 4 iterations in both stages of the RK method.

Example 4: Simulation of the full-3D appendage model. We finally turn to the simulation of the mechanochemical interaction in the context of skin appendage using a 3D slab as computational domain, and focusing on the reaction model proposed in (2.4). Model parameters are chosen according to Table 4.4. The domains of interest are the blocks $\Omega^D = (0, 50)^3$ and $\Omega^E = (0, 50)^2 \times (50, 75)$, which we discretise into unstructured meshes with 104360 and 60067 tetrahedral elements, respectively. Initial concentrations are set according to steady state solutions obtain from (2.4), perturbed with a uniformly

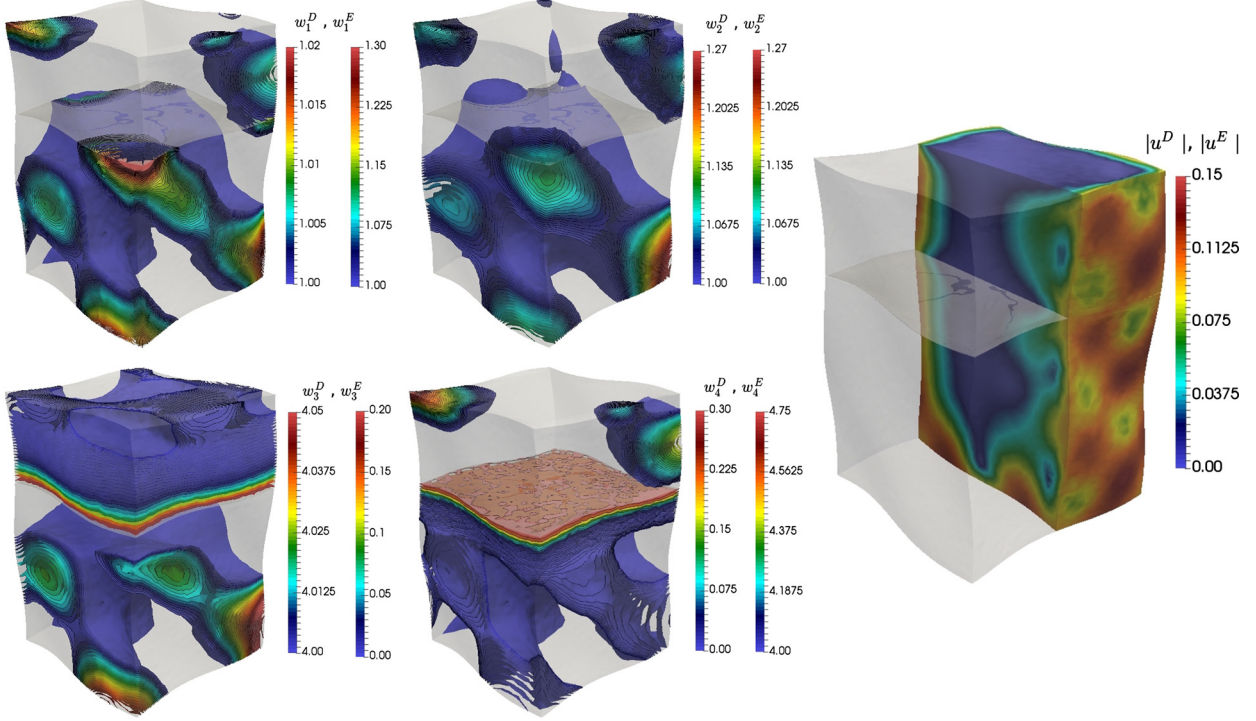


Fig. 4.11. Example 4, 3D case. Concentration of species w_1^* , w_2^* , w_3^* , w_4^* (left panels) and displacement magnitude (right), computed at $T = 300$ and plotted on the deformed configuration (scaled 10 times for better visualisation). For the displacement magnitude, we cut the domain in half to see the internal displacement.

distributed random variable with variance 10^{-3} . The adaptive method described in Algorithm 2 is employed with controller parameters as in Table 4.3, except for $A_{\text{TOL}} = 10^{-6}$ and $\text{TOL}_N = R_{\text{TOL}} = 10^{-3}$. The process is run until $T = 300$.

The results are presented in Fig. 4.11, showing a clear shift in species (cell, matrix and morphogens) concentration patterns across the interface, with the exception of species w_2^* (explained by the similarity in the reaction description (2.4)). The uniform Lamé constants on both domains and the Robin conditions imply that deformation patterns are of comparable magnitude throughout Ω , and the zones of high deformations are concentrated near the domain boundary. Different mechanochemical patterns can be produced by changing the coupling and reaction parameters, and a specific study on linear and nonlinear stability will be carried out in a forthcoming contribution. At this stage we can already observe that for w_1^* , for example, only the dermis species possesses a production term (with logistic growth) while the dynamics on the epidermis is described by a convection-diffusion process. This explains why the concentration variation in the dermis is much smaller than in the epidermis layer. For w_3^* and w_4^* we observe a similar behaviour, but having a larger variation on the z-axis for a specific layer (Ω^D for w_4 , Ω^E for w_3). This is due to some chemical species being produced only on a specific layer (see (2.4)) and the relevant concentration decreases rapidly, due to metabolism degradation, as one moves away from that layer.

5. Concluding remarks

We have introduced a mechanochemical model for the simulation of basic processes related to skin appendage patterning mechanisms. The two-way coupling between linear elasticity and advection-diffusion-reaction systems is achieved through a mechanical term depending on the gradient of the chemical species, and a pressure-dependent source term representing production of species. A weak formulation in a multidomain setting was introduced, and we presented a partitioned fixed-point and Schwarz algorithm to decouple the system into four principal blocks (the two domains, dermis and epidermis, being treated for advection-diffusion-reaction and mechanics). The space discretisation uses MINI-elements for the approximation of the displacement-pressure pair, and piecewise linear and continuous Lagrange elements for the species concentrations. A trapezoidal BDF2 method combined with adaptive Runge-Kutta schemes is used as a time advancing strategy, and algorithmic details are provided. The convergence properties of the proposed methods were studied in detail, and a set of numerical tests addresses pattern generation and the deformation of the interface.

Anomalous diffusivity was not considered here and can be readily incorporated. However, a deeper investigation is needed on the detailed linear stability analysis associated to the coupling mechanisms for the specific models at hand, as well as on the application of the developed methods in the simulation of more complex phenomena. Future work will also address extension of our model to non-linear elasticity and viscoelasticity and theoretical considerations on the con-

vergence properties of partitioned and monolithic schemes. Other possible lines of work include alternative approaches in the description of the interface problem itself. Also, using dedicated interface finite element methods designed for contact problems between two different materials and following a multi-field formulation as the one recently advanced in [29,30]. An advantage of such formalism is that local imperfections in the bonding sites can be described much more easily and their implementation can be done much in the same way as what we have proposed here. It nevertheless remains to see up to which extent these modifications have an impact on the qualitative and quantitative behaviour of the global coupled system.

References

- [1] L. Ahtainen, S. Lefebvre, P.H. Lindfors, E. Renvoisé, V. Shirokova, M.K. Virtainen, I. Thesleff, M.L. Mikkola, Directional cell migration, but not proliferation, drives hair placode morphogenesis, *Dev. Cell* 28 (5) (2014) 588–602.
- [2] R. Allen, J.J. Muñoz, D. Aubry, Diffusion–reaction model for *Drosophila* embryo development, *Comput. Methods Biomed. Eng.* 16 (3) (2013) 235–248.
- [3] B. Andreianov, M. Bendahmane, A. Quarteroni, R. Ruiz-Baier, Solvability analysis and numerical approximation of linearized cardiac electromechanics, *Math. Models Methods Appl. Sci.* 25 (05) (2015) 959–993.
- [4] D.N. Arnold, F. Brezzi, M. Fortin, A stable finite element for the Stokes equations, *Calcolo* 21 (1984) 337–344.
- [5] A. Badugu, C. Kraemer, P. Germann, D. Manshyuk, D. Iber, Digit patterning during limb development as a result of the BMP-receptor interaction, *Sci. Rep.* 2 (2012) 991.
- [6] R.E. Bank, W.M. Coughran Jr, W. Fichtner, E.H. Grosse, D.J. Rose, R.K. Smith, Transient simulation of silicon devices and circuits, *IEEE Trans. Comput.-Aided Des.* 4 (1985) 436–451.
- [7] R. Becker, E. Burman, P. Hansbo, A Nitsche extended finite element method for incompressible elasticity with discontinuous modulus of elasticity, *Comput. Methods Appl. Mech. Eng.* 198 (2009) 3352–3360.
- [8] F. BenBelgacem, L.K. Chilton, P. Seshaiyer, The hp -mortar finite-element method for the mixed elasticity and Stokes problems, *Comput. Math. Appl.* 46 (2003) 35–55.
- [9] L. Bonaventura, A. Della Rocca, Unconditionally strong stability preserving extensions of the TR-BDF2 method, *J. Sci. Comput.* 70 (2017) 859–895.
- [10] M. Buck, O. Iliev, H. Andrà, Multiscale finite element coarse spaces for the application to linear elasticity, *Cent. Eur. J. Math.* 11 (4) (2013) 680–701.
- [11] W. Chen, X. Xu, S. Zhang, On the optimal convergence rate of a Robin–Robin domain decomposition method, *J. Comput. Math.* 32 (4) (2014) 456–475.
- [12] G.C. Cruywagen, J.D. Murray, On a tissue interaction model for skin pattern formation, *J. Nonlinear Sci.* 2 (2) (1992) 217–240.
- [13] R. Dillon, H.G. Othmer, A mathematical model for outgrowth and spatial patterning of the vertebrate limb bud, *J. Theor. Biol.* 197 (1999) 295–330.
- [14] N. Di-Pòi, M.C. Milinkovitch, The anatomical placode in reptile scale morphogenesis indicates shared ancestry among skin appendages in amniotes, *Sci. Adv.* 2 (6) (2016).
- [15] V. Dolean, P. Jolivet, F. Nataf, *An Introduction to Domain Decomposition Methods. Algorithms, Theory, and Parallel Implementation*, SIAM, Philadelphia, PA, USA, 2015.
- [16] J.D. Edwards, J.E. Morel, D.A. Knoll, Nonlinear variants of the TR/BDF2 method for thermal radiative diffusion, *J. Comput. Phys.* 230 (2011) 1198–1214.
- [17] F. Hecht, New development in FreeFem++, *J. Numer. Math.* 20 (3–4) (2012) 251–265.
- [18] M.J. Gander, F. Magoules, F. Nataf, Optimized Schwarz methods without overlap for the Helmholtz equation, *SIAM J. Sci. Comput.* 24 (2002) 38–60.
- [19] G.N. Gatica, B. Gomez-Vargas, R. Ruiz-Baier, Analysis and mixed-primal finite element discretisations for stress-assisted diffusion problems, *Comput. Methods Appl. Mech. Eng.* 337 (2018) 411–438.
- [20] G.N. Gatica, W.L. Wendland, Coupling of mixed finite elements and boundary elements for a hyperelastic interface problem, *SIAM J. Numer. Anal.* 34 (6) (1997) 2335–2356.
- [21] A. Gierer, H. Meinhardt, A theory of biological pattern formation, *Kybernetik* 12 (1972) 30–39.
- [22] J.D. Glover, K.L. Wells, F. Matthäus, K.J. Painter, W. Ho, J. Riddell, J.A. Johansson, M.J. Ford, C.A.B. Jahoda, V. Klika, R.L. Mort, D.J. Headon, Hierarchical patterning modes orchestrate hair follicle morphogenesis, *PLoS Biol.* 15 (7) (2007) 1–31.
- [23] P. Gosselet, C. Rey, Non-overlapping domain decomposition methods in structural mechanics, *Arch. Comput. Methods Eng.* 13 (4) (2007) 515–572.
- [24] E. Hairer, S.P. Nørsett, G. Wanner, *Solving Ordinary Differential Equations I, Nonstiff Problems*, Springer Series in Computational Mathematics, Springer, New York, 2008.
- [25] E. Hairer, G. Wanner, *Solving Ordinary Differential Equations II, Stiff and Differential-Algebraic Problems*, Springer Series in Computational Mathematics, Springer, New York, 2010.
- [26] W.K.W. Ho, L. Freem, D. Zhao, K.J. Painter, T.E. Woolley, E.A. Gaffney, M.J. McGrew, A. Tzika, M. Milinkovitch, P. Schneider, A. Drusko, F. Matth'aus, J.L. Glover, K.L. Wells, J.A. Johansson, M.G. Davey, H.M. Sang, M. Clinton, Feather arrays are patterned by interacting signalling and cell density waves, *PLoS Biol.* (2019), in press.
- [27] M.E. Hosea, L.F. Shampine, Analysis and implementation of TR-BDF2, *Appl. Numer. Math.* 20 (1) (1996) 21–37.
- [28] T. Lecuit, P.-F. Lenne, Cell surface mechanics and the control of cell shape, tissue patterns and morphogenesis, *Nat. Rev. Mol. Cell Biol.* 8 (8) (2007) 633–644.
- [29] P. Lenarda, M. Paggi, A geometrical multi-scale numerical method for coupled hydro-thermo-mechanical problems in photovoltaic laminates, *Comput. Mech.* 57 (2016) 947–963.
- [30] P. Lenarda, A. Gizzi, M. Paggi, A modeling framework for electro-mechanical interaction between excitable deformable cells, *Eur. J. Mech. A, Solids* 72 (2018) 374–392.
- [31] P. Lenarda, M. Paggi, R. Ruiz-Baier, Partitioned coupling of advection-diffusion-reaction systems and Brinkman flows, *J. Comput. Phys.* 344 (2017) 281–302.
- [32] P.L. Lions, On the Schwarz alternating method. III: a variant for non-overlapping subdomains, in: T.F. Chan, R. Glowinski, J. Périaux, O. Widlund (Eds.), *Third International Symposium on Domain Decomposition Methods for Partial Differential Equations*, Held in Houston, Texas, March 20–22, 1989, Philadelphia, PA, SIAM, 1990.
- [33] R.T. Liu, S.S. Liaw, P.K. Maini, Two-stage Turing model for generating pigment patterns on the leopard and the jaguar, *Phys. Rev. E* 74 (1) (2006) 011914.
- [34] D. Manoussaki, A mechanochemical model of angiogenesis and vasculogenesis, *ESAIM: Math. Model. Numer. Anal.* 37 (04) (2003) 581–599.
- [35] M. Mercker, F. Brinkmann, A. Marciniak-Czochra, T. Richter, Beyond Turing: mechanochemical pattern formation in biological tissues, *Biol. Direct* 11 (1) (2016) 22–37.
- [36] S.E. Millar, Molecular mechanisms regulating hair follicle development, *J. Invest. Dermatol.* 118 (2) (2002) 216–225.
- [37] S.A. Montandon, A.C. Tzika, A.F. Martins, B. Chopard, M.C. Milinkovitch, Two waves of anisotropic growth generate enlarged follicles in the spiny mouse, *EvoDevo* 5 (2014) 33.
- [38] P. Moreo, E.A. Gaffney, J.M. García-Aznar, M. Doblaré, On the modelling of biological patterns with mechanochemical models: insights from analysis and computation, *Bull. Math. Biol.* 72 (2010) 400–431.

- [39] J.D. Murray, G.F. Oster, Generation of biological pattern and form, *IMA J. Math. Appl. Med. Biol.* 1 (1) (1984) 51–75.
- [40] J.D. Murray, P.K. Maini, R.T. Tranquillo, Mechanochemical models for generating biological pattern and form in development, *Phys. Rep.* 171 (2) (1988) 59–84.
- [41] J.D. Murray, *Mathematical Biology II: Spatial Models and Biomedical Applications*, Interdisciplinary Applied Mathematics, Springer, New York, 2006.
- [42] T. Oliver, J. Lee, K. Jacobson, Forces exerted by locomoting cells, *Biol. Cell* 5 (3) (1994) 139–147.
- [43] G.F. Oster, J.D. Murray, A.K. Harris, Mechanical aspects of mesenchymal morphogenesis, *Development* 78 (1) (1983) 83–125.
- [44] M. Pawlaczyk, M. Lelonkiewicz, M. Wieczorowski, Age-dependent biomechanical properties of the skin, *Postepy. Dermatol. Alergol.* 30 (5) (2013) 302–306.
- [45] M. Ptashnyk, B. Seguin, Homogenization of a system of elastic and reaction–diffusion equations modelling plant cell wall biomechanics, *ESAIM: Math. Model. Numer. Anal.* 50 (2) (2016) 593–631.
- [46] L. Qin, X. Xu, Optimized Schwarz methods with Robin transmission conditions for parabolic problems, *SIAM J. Sci. Comput.* 31 (2008) 608–623.
- [47] A. Quarteroni, T. Lassila, S. Rossi, R. Ruiz-Baier, Integrated Heart – Coupling multiscale and multiphysics models for the simulation of the cardiac function, *Comput. Methods Appl. Mech. Eng.* 314 (2017) 345–407.
- [48] R. Ruiz-Baier, Primal-mixed formulations for reaction–diffusion systems on deforming domains, *J. Comput. Phys.* 299 (2015) 320–338.
- [49] S. Sick, S. Reinker, J. Timmer, T. Schlake, WNT and DKK determine hair follicle spacing through a reaction–diffusion mechanism, *AAAS* 314 (5804) (2006) 1447–1450.
- [50] L.J. Shaw, J.D. Murray, Analysis of a model for complex skin patterns, *SIAM J. Appl. Math.* 50 (2) (1990) 628–648.
- [51] H. Shoji, A. Mochizuki, Y. Iwasa, M. Hirata, T. Watanabe, S. Hioki, S. Kondo, Origin of directionality in the fish stripe pattern, *Dev. Dyn.* 226 (4) (2003) 627–633.
- [52] A.E. Shyer, A.R. Rodrigues, G.G. Schroeder, E. Kassianidou, S. Kumar, R.M. Harland, Emergent cellular self-organization and mechanosensation initiate follicle pattern in the avian skin, *Science* 357 (6353) (2017) 811–815.
- [53] G. Söderlind, Automatic control and adaptive time-stepping, *Numer. Algebra* 31 (1) (2002) 281–310.
- [54] A. Tosin, Mechanics and chemotaxis in the morphogenesis of vascular networks, *Bull. Math. Biol.* 68 (7) (2006) 1819–1836.
- [55] L. Tranqui, P. Tracqui, Mechanical signalling and angiogenesis. The integration of cell-extracellular matrix couplings, *C. R. Acad. Sci.* 323 (1) (2000) 31–47.
- [56] A.M. Turing, The chemical basis of morphogenesis, *Philos. Trans. R. Soc. Lond. A* 237 (1990) 37–72.
- [57] M.A. Wyżczałkowski, Z. Chen, B.A. Filas, V.D. Varner, L.A. Taber, Computational models for mechanics of morphogenesis, *Birth Defects Research* 92 (6) (2012) 132–152.
- [58] B. Wang, K. Xia, G.W. Wei, Matched interface and boundary method for elasticity interface problems, *J. Comput. Appl. Math.* 285 (2015) 203–225.